Gondwana Research 151 (2026) 206–231

Contents lists available at ScienceDirect

Gondwana Research

journal homepage: www.elsevier.com/locate/gr

Research Paper

Seismically triggered anoxia and brine spillover during the CE 365 Crete mega-earthquake in the eastern Mediterranean Sea

A. Polonia [a,*], A. Asioli [a], L. Ferraro [a], E. Colizza [b], F. Corticelli [c], G.J. de Lange [d], A. Gallerani [a], G. Gasparotto [e], L. Gasperini [a], G. Giorgetti [a], V. La Cono [f], G. La Spada [f], T. Tesi [f], M. Yakimov [f]

[a] Istituto di Scienze Marine (ISMAR-CNR), Consiglio Nazionale delle Ricerche, Italy
[b] Dip. di Matematica, Informatica e Geoscienze, Università degli Studi di Trieste, Italy
[c] Institute for Microelectronics and Microsystems (IMM-CNR), Consiglio Nazionale delle Ricerche, Italy
[d] Department of Earth Sciences – Geochemistry, Faculty of Geosciences, Utrecht University, Netherlands
[e] Department of Biological, Geological and Environmental Sciences, University of Bologna, Bologna, Italy
[f] Istituto di Scienze Polari, Consiglio Nazionale delle Ricerche, Italy

ARTICLE INFO

Keywords:
Hellenic Arc
Crete CE 365 mega-earthquake
Brine lakes
Mediterranean ridge accretionary complex
Seafloor anoxia and brine formation

ABSTRACT

The Hellenic Arc subduction system hosts unique brine-filled depressions that represent the world's deepest and most hypersaline basins currently characterized by anoxic sedimentation and gypsum precipitation. Their origin is intimately linked to active tectonics and to the presence of Messinian evaporites in the sub-seafloor, but the formation processes are not fully understood. Understanding how they developed and the triggering mechanism for brine formation can provide valuable information about their evolution and the past history of such extreme environments on Earth and extraterrestrial analogues.

We conducted sediment coring and direct sampling of the brine lake Hephaestus to reconstruct the sedimentary and environmental characteristics of the basin. We found that the basin preserves a stratigraphy spanning at least 200 kyr and contains a combination of pelagic sediment and resedimented deposits. Sediment stratigraphy records the transition from oxic sediment at the core bottom to recent anoxic conditions marked by black viscous sediment. This transition is punctuated by multi-sourced slumped material that was emplaced during a catastrophic event capable of simultaneously triggering deep sea slope failures and turbidity currents from the coastal environment. Radiometric dating and age modeling suggest that sediment anoxia resulted from catastrophic sediment remobilization that occurred sometime in the time interval CE 155-439. This is consistent with the CE 365 M>8 Crete earthquake and related mega-tsunami. We propose that seismic shaking triggered slope failures, turbidity currents and large-amplitude waves of the brine interface in the neighboring anoxic Kryos basin with brine spillover from one basin into deep depression(s).

1. Introduction

Deep-sea brine lakes form through the accumulation of hypersaline solutions into seabed depressions within salt basins such as the Mediterranean Sea, the Gulf of Mexico, and the Red Sea (Aharon et al., 1992; Cita, 2006; Purkis et al., 2022 and references therein). Despite their limited size, brine lakes are of intense scientific interest because they represent one of the most extreme environments on Earth, offering analogues for understanding early Earth conditions (Van Der Wielen et al., 2005), potential life on other planets (Mancinelli et al., 2004), origin of hydrocarbon-rich black shales, and microbial enzymes and secondary metabolites for biotechnological applications (Ferrer et al., 2005; Sagar et al., 2013; Varrella et al., 2020; Ziko et al., 2019).

The world's deepest and most hypersaline (between 5 and 10 times higher than the salinity of seawater) anoxic basins are located on peculiar depressions of the Mediterranean Ridge accretionary complex in the Eastern Mediterranean Sea (Fig. 1). Their formation appears to be controlled by the interaction of active tectonics, the exhumation and dissolution of Messinian evaporites by seawater (Camerlenghi and Cita, 1987) and the upwards advection of fossil relict brines (Vengosh et al., 1998). The location of brine lakes in tectonically active belts of the Hellenic Arc subduction complex, where surficial sediment deformation

* Corresponding author.
E-mail address: alina.polonia@ismar.cnr.it (A. Polonia).

https://doi.org/10.1016/j.gr.2025.10.016
Received 1 April 2025; Received in revised form 13 October 2025; Accepted 14 October 2025
Available online 16 November 2025

allows evaporites and fluids to be transported to the seafloor, provides clear evidence of the interplay between tectonics and formation of anoxic basins (Jongsma, 1987). However, the specific type of triggering mechanism causing brine accumulation in the confined depressions remains unclear.

This paper focuses on the study of sediment samples from the Hephaestus basin, the youngest brine lake on Earth (La Cono et al., 2019), with the final aim of tracking the transition from oxic to anoxic conditions of the basin floor and reconstructing: i) sedimentary processes associated with brine formation; ii) age of brines; iii) triggering mechanisms for seafloor anoxia. We found that tectonic activity in the Hellenic Arc and seismic shaking play a fundamental role in triggering sediment remobilization, basin floor anoxia and brine formation/spillover.

2. Tectonic setting

The Hellenic Arc in the eastern Mediterranean Sea accommodates African Plate subduction beneath the continental Eurasian Plate at rates ranging from 26 to 34 mm/yr (McClusky et al., 2000). This has produced a structurally complex subduction system that comprises the Mediterranean Ridge salt bearing accretionary wedge, the inner plateau (a Messinian forearc basin) above the continental backstop, and the Hellenic trough to the NE (Mouslopoulou et al., 2025) (Fig. 1).

The external Mediterranean Ridge shows a very low taper (~2°) consistent with an extremely low basal friction and fluid overpressuring on the basal detachment (Reston et al., 2002). Variations in the accretionary wedge geometry are related to different stages of continental collision (Polonia et al., 2002), lateral variations in evaporite thickness and to local relief on the subducting plate enhancing fluid escape from beneath the evaporites (Reston et al., 2002). Shortening and sediment deformation is taken up along arc parallel thrust faults and shear zones bounding longitudinally the different structural domains (Mouslopoulou et al., 2025). Some of these major structural elements detach on the ductile Messinian evaporites with associated halokinetic processes (Polonia et al., 2002). Despite the high proportion of aseismic deformation (Saltogianni et al., 2020; Shaw et al., 2008; Vernant et al., 2014), devastating earthquakes (> M8) and associated tsunamis have been generated along the Hellenic Arc (Guidoboni and Comastri, 1997; Papadopoulos, 2011), such as the CE 365 M~8.5 event (Pirazzoli et al., 1996, 1982; Shaw et al., 2008; Stiros, 2001) and CE 1303 M~8.0 earthquake in western and eastern Crete respectively (Papadopoulos, 2011) (Fig. 1).

The Mediterranean Ridge and inner plateau host several isolated and confined anoxic basins filled with hypersaline brines (Fig. 1). The brine lakes develop in different structural settings, including a deformed area related to a continental seamount approaching the subduction zone (Bannock Basin) (Cita et al., 1985; von Huene and Ranero, 2003), a pull apart basin in the western Strabo Trough (Tyro Basin) (Erba et al., 1987a; Jongsma, 1987; Ten Haven et al., 1985), and a complex supra-backstop setting in the inner plateau (Cita, 2006). The majority of the brine lakes are located near the crest of the Mediterranean Ridge

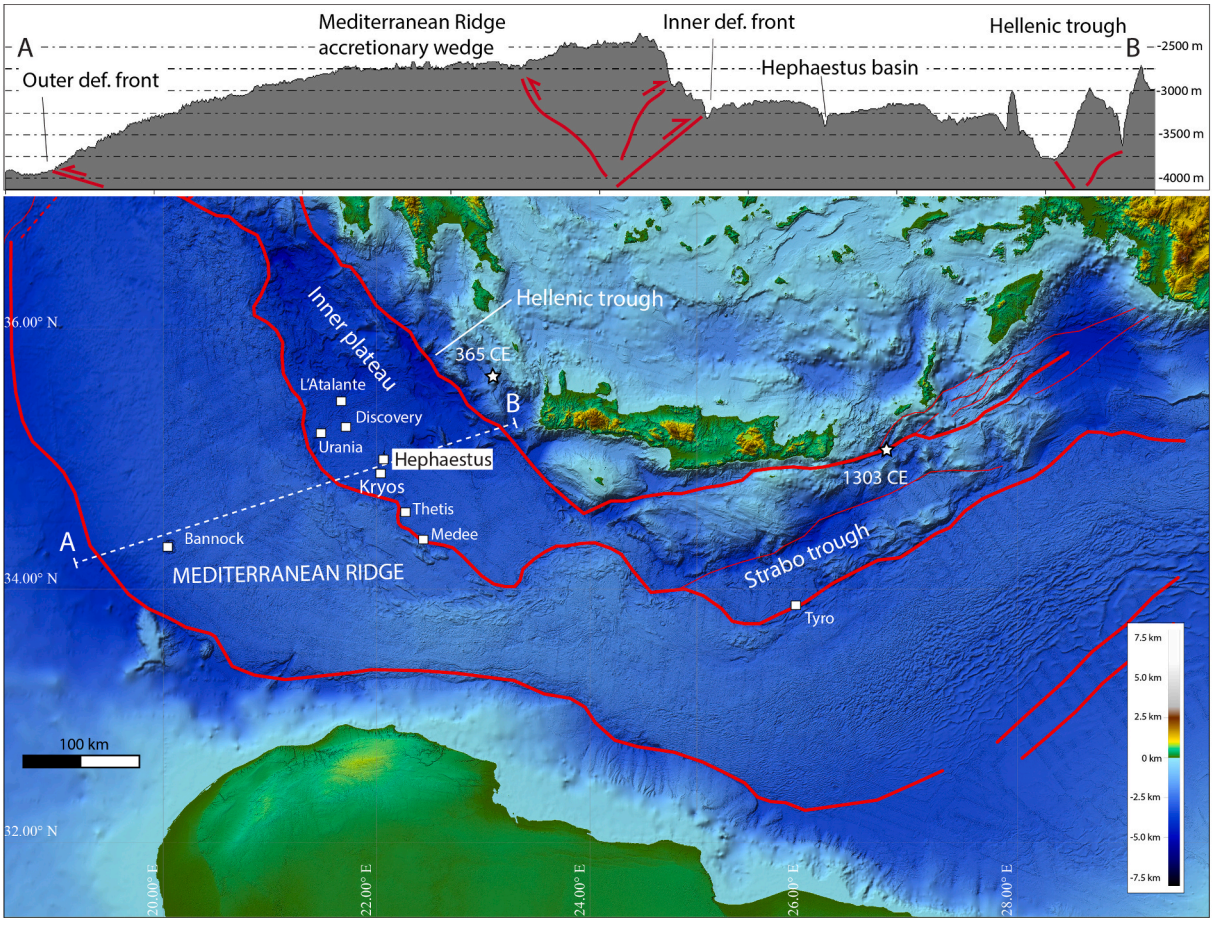

Fig. 1. Location map of the brine lakes and tectonic/geodynamic context within the different structural domains of the Hellenic Arc subduction system (Mediterranean Ridge accretionary wedge, Inner plateau, Hellenic and Strabo Troughs). The epicenters of the CE 365 and CE 1303 Crete earthquakes are indicated by the white stars. The different anoxic basins are indicated by a white square. A-B: cross section showing the different domains of the Hellenic Arc subduction system and major faults accommodating Africa-Eurasia plate convergence. Red lines: major faults accommodating Africa-Eurasia plate convergence in the subduction complex. (For interpretation of the references to color in this figure legend, the reader is referred to the web version of this article.)

(MEDRIFF Consortium, 1995), at the transition between the inner plateau and the accretionary wedge that occurs along the inner deformation front of the subduction system (Fig. 1), where a major dextral flower structure is associated with massive mud expulsion (Chamot-Rooke et al., 2005). In the neighboring Calabrian Arc, mud volcanoes and fluid flow related features occur in a similar setting (Panieri et al., 2013). A post-Pliocene kinematic reorganization changed the tectonic regime at the prism-backstop boundary from compressive to highly sheared (Kreemer and Chamot-Rooke, 2004) and the portions of the subduction system under strike-slip regime appear to be efficiently vented sites (Behrmann, 1991). This scenario is compatible with pressure building during the compressive stage and mud and fluid escape following the wrench stage, in agreement with the young age (1–2 Ma) of the Mediterranean mud volcanoes (Chamot-Rooke et al., 2005 and references therein).

3. Brine lakes in the Mediterranean Ridge accretionary complex

The Tyro and Bannock basins were the first brine lakes to be discovered in 1983–1984 (Cita et al., 1985; de Lange et al., 1990; de Lange and ten Haven, 1983; Jongsma et al., 1983). The Tyro basin is located in the Western Strabo Trough, where Messinian evaporites are offset by fault scarps (Erba et al., 1987a; Jongsma, 1987). The Bannock Basin forms in the external part of the Mediterranean Ridge, where a topographic relief disrupted the sedimentary cover and opened a window through which evaporites and fluids could exit to the seafloor (von Huene et al., 1997). Several complexes of brine lakes (Urania, Discovery, L'Atalante, Thetis, Medee, Kryos, and Hephaestus) (Fig. 1) were discovered at the prism-backstop contact (La Cono et al., 2019, 2011; MEDRIFF Consortium, 1995; Yakimov et al., 2015; Yakimov et al., 2013) while a shallower (~1150 m water depth) brine lake was described offshore Israel (Herut et al., 2022). Other minor brine lakes are associated with large mud volcanoes on the crest of the Mediterranean Ridge or in the Nile deep-sea fan (Dählmann and de Lange, 2003; Dupré et al., 2014; Woodside and Volgin, 1996).

The Hellenic Arc brine lakes behave as different hydrologic systems with different geometries and brine composition. Some of these basins are horse-shaped with a central conical hill surrounded by a number of depressions of variable shape and depth (Urania, Bannock, Atalante), others show sub-circular troughs (Tyro, Discovery, Thetis) while some of them are elongated depressions following major tectonic boundaries and/or structural lineaments of the Mediterranean Ridge (Kryos, Medee, Hephaestus). The anoxic basins sizes range from few km (Atalante, Thetis, Tyro) to more than 25 km (Medee) while the vertical relief between the depressions and the surrounding steep slopes is hundreds of meters. The maximum thickness of the high-density brines varies from 30 m to 500 m in the Bannock basin (Cita, 2006), while the depth of the interface between high-density brines and seawater ranges from −3200 m (Bannock) to −3455 m (Urania).

The composition of brines varies in the different basins depending on the lithology and distribution of different Messinian suite layers (Cita, 2006). Some brines (i.e., Discovery, Kryos and Hephaestus), were attributed to the dissolution of Mg evaporites, mainly bishofite (La Cono et al., 2019; Wallmann et al., 1997). Urania and Bannock brines are related to either the dissolution of Messinian evaporites or the relics of fossil evaporated seawater entrapped in the sediments (Cita, 2006; de Lange et al., 1990; Vengosh et al., 1998). Tyro is strongly enriched in sodium (5300 mmol/L), suggesting a derivation from the halite which is characteristic of the uppermost levels of the evaporitic suite (Cita, 2006). L'Atalante is a thalassohaline basin similar to Thetis (La Cono et al., 2011).

The existence of brines in the Hephaestus basin was confirmed by direct conductivity-temperature-dissolved oxygen (CTD) profiling, and by direct sampling (La Cono et al., 2019). The upper surface of the Hephaestus brine is located at 3373 m, some 36 m lower than that of Lake Kryos, just few km distance. Chemical characterization of Hephaestus brine confirmed that these two lakes constitute separate hydrologic systems, although Hephaestus shares the athalassohaline character of the Kryos and Discovery brines (La Cono et al., 2019).

4. Materials and methods

In this section, we provide the most important information on applied methodologies (Table 1). Further details are reported in the SM1.

4.1. Geophysical data

Morphobathymetric maps were obtained from multibeam swath bathymetry collected onboard R/V CNR Urania in 2012 with a Kongsberg-Simrad EM-302 echosounder. Raw data were processed obtaining a 5 m resolution bathymetric grid. Chirp data were collected using a 15 transducers Benthos Chirp III system.

4.2. Sediment coring

The gravity core KR2_2 was collected in the Hephaestus basin at 3398 m water depth during the CNR-Urania SALINE cruise carried out in 2014. The core was scanned by a medical Core axial Tomography (CT) scan system, under *X-ray* energy of 120 kV and pitch of 0.3. High-resolution magnetic susceptibility (MS) logs were acquired with a *Bartington*, model MS2, equipped with a 100 mm loop sensor at a sampling interval of 5 mm.

4.3. X-ray Fluorescence (XRF core scanner)

Geochemical data were collected by using an *Avaatech* XRF-CS at ISMAR CNR-Bologna, under 10 kV, 30 kV and 50 kV (10, 20 and 35 s measuring time respectively) settings, with a step size of 5 mm along the cores. Elemental concentrations of XRF data in the figures and text are count-based estimates of elemental abundance.

4.4. Grain size

Grain-size analyses were performed on 80 samples with a varying sampling rate (1–6 cm). Sediment textures were analyzed using a laser MALVERN Mastersizer, for size ranges between 0.02 and 2000 μm. Results were classified according to Friedman and Sanders (1978) grain-size scale and are presented as % in sand, silt, clay and median particle size (Md) expressed in μm.

4.5. Carbon and nitrogen analysis

Total nitrogen (TN), organic carbon (OC), inorganic carbon (IC) and stable carbon isotopes of OC ($\delta^{13}C$) were analysed using a Thermo Fischer Scientific DELTA Q mass spectrometer coupled with a Thermo Fisher Scientific FLASH 2000 Elemental Analyser via a Conflo IV (EA-IRMS). For the OC, about 25 mg of samples were weighed in silver cups and acidified with 1.5 M HCl to remove the inorganic carbon. IC was determined as difference between total carbon (untreated) and OC. For total carbon and TN, sediments were weighed in tin cups (about 25 mg) prior to the analysis. TN, OC and IC contents are reported as weight % of the bulk sediment. Standard deviation for $\delta^{13}C$ values is better than 0.1 ‰ based on replicates on in-house standards. OC/TN ratio refers to the molar ratio.

4.6. Biomarkers

We employed microwave-assisted alkaline CuO oxidation following Goñi and Montgomery (2000) (SM1 and SM2). The resulting extracts were acidified, extracted with ethyl acetate, dehydrated, and prepared for gas chromatography-mass spectrometry (GC-MS) analysis. CuO

Table 1
Summary list of the methods used, the number of samples used per method, the material used for each analysis and the general aim of each method.

Method/Type of analysis	N° of Samples	Material/Matrix	Information
Grain size	80	Bulk sediment (2 g ca.)	Sediment texture, particle size
X-Ray Fluorescence (XRF core scanner)	0,5 cm sampling interval	Bulk sediment (half-core)	Major and trace elemental profiles, redox conditions, organic productivity, water mass change, sedimentological events (turbidites), facies interpretation
Organic Carbon (OC)	70	Dry sediment acidified before the analysis (26 mg)	Sediment properties
$\delta^{13}C$	70	Dry sediment acidified before the analysis (27 mg)	Sediment source
Biomarkers	24	Bulk sediment (100–300 mg, depending on the OC content)	Sediment source
Planktic foraminifera	25	Sediment fraction > 0.106 mm	Biostratigraphy, climate cyclicity, paleoenvironment
Benthic foraminifera	54	Sediment fraction > 0.063 mm	Paleobathymetry, paleoenvironment
Mineralogy (stereomicroscope)	60	Dry samples	Sediment composition
Mineralogy (SEM-EDS)	10	Selected grains (handpicked after stereomicroscope examination)	Minerals identification
Radiometric dating (^{14}C)	7	$CaCO_3$ shells (Planktic foraminifera)	Chronology
Radiometric dating (^{14}C)	4	Bulk sediment (acid-insoluble organic matter)	Chronology
$18O/^{16}O$	30	Bulk brine and sediments pore water	Origin of basins
$D/^{1}H$	30	Bulk brine and sediments pore water	Origin of basins
RNA/cDNA	6	Seawater/brine interface	Biodiversity of metabolic active microbiota
Next Generation Sequencing	6	Seawater/brine interface	Biodiversity of metabolic active microbiota

oxidation is widely used to analyze lignin and cutin biomarkers, which serve as molecular tracers of terrestrial plant input and help constrain sources and diagenetic processes of organic matter in marine sediments in modern and ancient systems (Tesi et al. 2007; Tesi et al., 2016). Lignin phenols (vanillyl, syringyl, cinnamyl) were quantified to trace terrestrial plant material contributions to organic matter (OM). Ratios like S/V (angiorsperm vs gymnosperm tissues) and C/V (soft vs woody tissues) provided insights into plant types. Upon CuO oxidation, cutin-derived hydroxy fatty acids which belong to the family of wax lipids are produced and serve as additional land-derived proxies. Finally we carried out hydrocarbon analyses targeting the viscous sediment sections to test the potential source from oil-derived material, employing alkaline hydrolysis and liquid–liquid extraction. GC-MS analysis of n-alkanes (C_{22}–C_{34}) was then used to assess the organic matter maturity through the Carbon Preference Index (CPI). Low CPI values indicated oil or kerogen influence, while higher values pointed to fresh terrestrial input. These methods characterized organic matter origins and degradation in marine sediment samples.

4.7. Foraminifera

4.7.1. Planktic foraminifera

Twenty-four sediment sub-samples were taken from the uppermost and the lowermost part of the core KR02_2 for stratigraphic and paleoenvironmental purpose. The samples were dried at 50 °C and washed through a 0.063 mm mesh sieve. The fraction > 0.106 mm was counted for the planktic foraminifera content in the lowermost part of the core. For the other samples a semi-quantitative analysis was performed. For counting each subsample has been split into aliquots using a Jones-type microsplitter and for each sample enough aliquots were counted to reach 300–500 specimens. The results, expressed as percentages, are reported in SM3.

4.7.2. Benthic foraminifera

Benthic foraminifera analyses were carried out on a total of fifty-four samples. The samples were dried at 50 °C and washed through a 0.063 mm mesh sieve. The fraction > 0.063 mm has been counted for the benthic foraminifera content (SM4). Foraminiferal benthic counts were performed considering only well-preserved specimens and data were reported as relative abundance (%) and as densities (FD = number of specimens/g of total sediment).

4.8. Mineralogical analysis

Mineralogical analyses were carried out on 60 selected samples to define sediment composition and sources using Stereo Microscope (Zeiss STEMI, AXIO software), SEM (Scanning Electron Microscope) with EDS (Energy Dispersive Spectroscopy) attachment, and XRD (X-Ray Diffraction). Stereomicroscope allowed the identification of the main components (minerals and plant fragments), SEM/EDS and XRD were used to estimate proportions among components and identify minerals.

4.9. Sediment pore water

Stable isotopes of oxygen and hydrogen ($^{18}O/^{16}O$ and $D/^{1}H$) were analyzed in brine and sediment pore water samples as described elsewhere (La Cono et al., 2019). Briefly, water from sediment samples was extracted using cryogenic water extraction protocol, optimized for clayey soils (Orlowski et al., 2018). Extracted pore water samples, brine and interface samples from Hephaestus and the overlying basin seawater were analyzed using an Isotope Ratio Mass Spectrometry (IRMS) system containing a reactor filled with “glassy carbon” granulate (2.00–3.15 mm) and nickel-coated carbon (IVA Analyzentechnik, Meerbusch, Germany) at 1480 °C. After pyrolysis of water, CO_2, CO and H_2 were separated at 95 °C and transferred to a Finnigan MAT 253 IRMS (ThermoFisher Scientific, Bremen, Germany). Results are presented in $^{18}O/^{16}O$ and $D/^{1}H$ isotopic ratios of water (expressed as $\delta^{18}O\text{-}H_2O$ and $\delta D\text{-}H_2O$ in ‰ vs. Vienna Standard Mean Ocean Water [V-SMOW]), indicating the concentration deviation in parts per thousand from the V-SMOW. Analytical errors for $\delta^{18}O\text{-}H_2O$ and $\delta D\text{-}H_2O$ were ±1 ‰ and ±0.1 ‰, respectively.

4.10. Biomolecular analyses

Total RNA was extracted from Hephaestus interface samples to study the metabolically active microbiota. RNA was converted to complementary DNA (cDNA), following a protocol by La Cono et al. (2019). The biodiversity of this unique, polyextreme environment was then investigated using Next-Generation Sequencing (NGS). The V3-V4 hypervariable regions of the SSU rRNA gene were amplified with the 341F/785R primer pair (Herlemann et al., 2011). The amplicons were sequenced on an Illumina MiSeq platform at FISABIO (https://fisabio.san.gva.es/en/servicios) in Valencia, Spain, using standard library preparation protocols (Caporaso et al., 2012). Raw reads were first

cleaned by removing barcodes and primers. Reads shorter than 150 bp, containing ambiguous bases, or exhibiting homopolymer runs longer than six nucleotides were discarded. The filtered reads were then imported into RStudio (R Core Team, 2022) and analyzed using the dada2 package (v1.26.0; Callahan et al., 2016), following the pipeline described in Cordone et al. (2022). Due to preprocessing performed by the sequencing facility (FISABIO), reads were trimmed using modified filtering parameters (truncLen = c(280, 280), maxN = 0, truncQ = 0, rm.phix = TRUE) as recommended by Crisafi et al. (2022). A parametric error model was applied to correct PCR-induced biases by optimizing convergence between error rate estimates and sample composition inference (Callahan et al., 2016). Paired-end reads were merged, and amplicon sequence variants (ASVs) were constructed. Chimeric sequences were identified and removed. Taxonomy was assigned to ASVs using a naïve Bayesian classifier against the SILVA database version 138 (v138; https://www.arb-silva.de/documentation/release-138/, https://zenodo.org/record/4587955#.YgKJlb_MJH4). Alpha diversity analyses, based on 16S rRNA sequence abundance, were performed using the Phyloseq and Microbiome packages in RStudio (McMurdie and Holmes, 2013; Shetty and Lathi, 2019; R Core Team, 2022). Diversity was assessed through Chao1, Shannon, and Simpson indices across the sampled sites.For phylogenetic analysis, aligned sequences were used to generate trees via the neighbor-joining algorithm in the ARB software package, based on distance analysis of 16S rRNA. Tree topology robustness was evaluated through bootstrap resampling (1000 replicates) using the same distance model. Additionally, phylogenetic trees were inferred using the PhyML plugin (v3.3.20180621) within Geneious Prime® 2024.0.5, applying the JC69 substitution model and 1000 bootstrap replicates. Nitrososphaerota sequence (MF624699) was employed as the outgroup for the archaeal tree, while a nanohaloarchaeal sequences (CP040089 and CP104395) served as the outgroup for the bacterial tree.

4.11. Radiometric dating

Accelerator mass spectrometry (AMS) radiocarbon dating of hand-picked planktonic foraminifera with no evidence of carbonate overgrowth or pyritization was performed. We selected samples in the pelagic units and within the slump deposit. About 5–6 mg of specimens (mixed or monospecific when possible) > 125 μm in size were studied. We also dated from sediment bulk OC a black patch included in the basal part of a resedimented deposit and we obtained ages from two different samples at the base of the anoxic sediment (Table 2).

4.12. Age modeling

We used the information we have about the deposition process in the upper part of the core to refine our chronologies (Section 6.3). The age model is built using the P_Sequence (a Bayesian model of deposition) implemented in the computer program OxCal 4.4 (version 175, 2024-11-07) that assimilates sedimentation as a random process following a Poisson law (Bronk Ramsey, 2008). The input parameters to generate the P_Sequence model are the uncalibrated ^{14}C ages and respective ΔR with their corresponding corrected depths. The regularity of sedimentation is determined by the k parameter with the higher values of k reflecting smaller variations in sedimentation rate (Bronk Ramsey, 2008). For our purposes we chose ΔR = 0 because no data are available for the study region, and k = 3.0 because we assume that sedimentation within the anoxic topmost sediment unit is rather constant. The model finally calculates the age of each corrected depth and generates the 95.4 % probability age ranges (2σ) for the turbidite bed emplacement process.

Table 2
Summary of AMS radiometric data performed on core KR2_2 with their corresponding depth in the cores, sediment unit, laboratory number, uncalibrated age. Column 6 represents calibrated ages with ΔR = 0. Column 7: type of material used for radiometric dating.

Core	cm bsf	Unit	Lab. No.	Age (^{14}C yr BP)	Age calibrated (ΔR = 0)	Remarks
KR2_2	17	E2	Poz-171471	2005 ± 30 BP	CE 418–673	Sediment bulk OC
KR2_2	21	E1	Poz-162274	2700 ± 30 BP	BCE 416-CE 112	Sediment bulk OC
KR2_2	84	D1	Poz-77959	7850 ± 50 BP		Sediment bulk OC (bishofite fragment)
KR2_2	84	D1	Poz-171473	47000 ± 3000 BP		Sediment bulk OC (black sediment)
KR2_2	130	C	Poz-103382	38000 ± 600 BP		*Globigerinoides ruber*
KR2_2	165	C	Poz-103381	48000 ± 3000 BP		*Globigerina bulloides*
KR2_2	256	S6	Poz-103379	>53000 BP		*Globigerina bulloides*
KR2_2	263	A	Poz-103378	>49000 BP		*Globigerinoides ruber*
KR2_2	274	S7	Poz-103377	>47000 BP		*Globigerinoides ruber*
KR2_2	289	A	Poz-103376	>54000 BP		*Globigerinoides ruber*
KR2_2	294	A	Poz-103375	>51000 BP		*Globigerinoides ruber*

5. Results

5.1. Tectonic and depositional setting based on geophysical data

Lake Hephaestus develops along a steep NNE-SSW oriented fracture between the inner deformation front of the subduction complex and the Hellenic Trough (Figs. 1 and 2). The central depression is approximately 3 km long and 0.7 km wide and has a maximum depth of 3423 m, 220–250 m deeper in relation to the surrounding seabed (Fig. 1). The Hephaestus basin shows a single confined depression to the North that bifurcates to the south. The depression is not fed by canyon systems and remains completely disconnected from the continental shelf.

Multibeam data reveal a complex morphology characterized by several confined basins aligned along the fracture within a very rough seafloor with many depressions and intervening structural highs. The Kryos basin to the South is about 10 km long and 0.3–1 km wide and is characterized by a rather rectilinear western margin while to the East, basin geometry is irregular with many lake secondary branches. The Hephaestus and Kryos basins are separated by a bathymetric sill about 200 m shallower than the Kryos depocenter (Fig. 2). Bathymetric profiles across the basin depocenters (Fig. 2) illustrate the depression's geometry and the brine-water interface at 3373 m in the Hephaestus basin and 3337 m in the Kryos basin as deduced through CTD data (La Cono et al., 2019) and Chirp profiles (Fig. 3). Multibeam data show evidence of slump deposits and mass wasting features within the Kryos depression and morphological breaks of the Hephaestus basin margins suggesting slope instability processes (SM5).

Chirp profiles collected along the basin axis are characterized by the presence of diffraction hyperbola from surrounding highs that hampers the possibility to clearly reconstruct seafloor morphology because of lateral seismic arrivals. In some regions, it is possible to identify the sharp seismic reflector corresponding to the interface between seawater and brines (Fig. 3B). The profiles show that the brine interface in the Kryos basin is about 35 m shallower relative to the Hephaestus basin (Fig. 3).

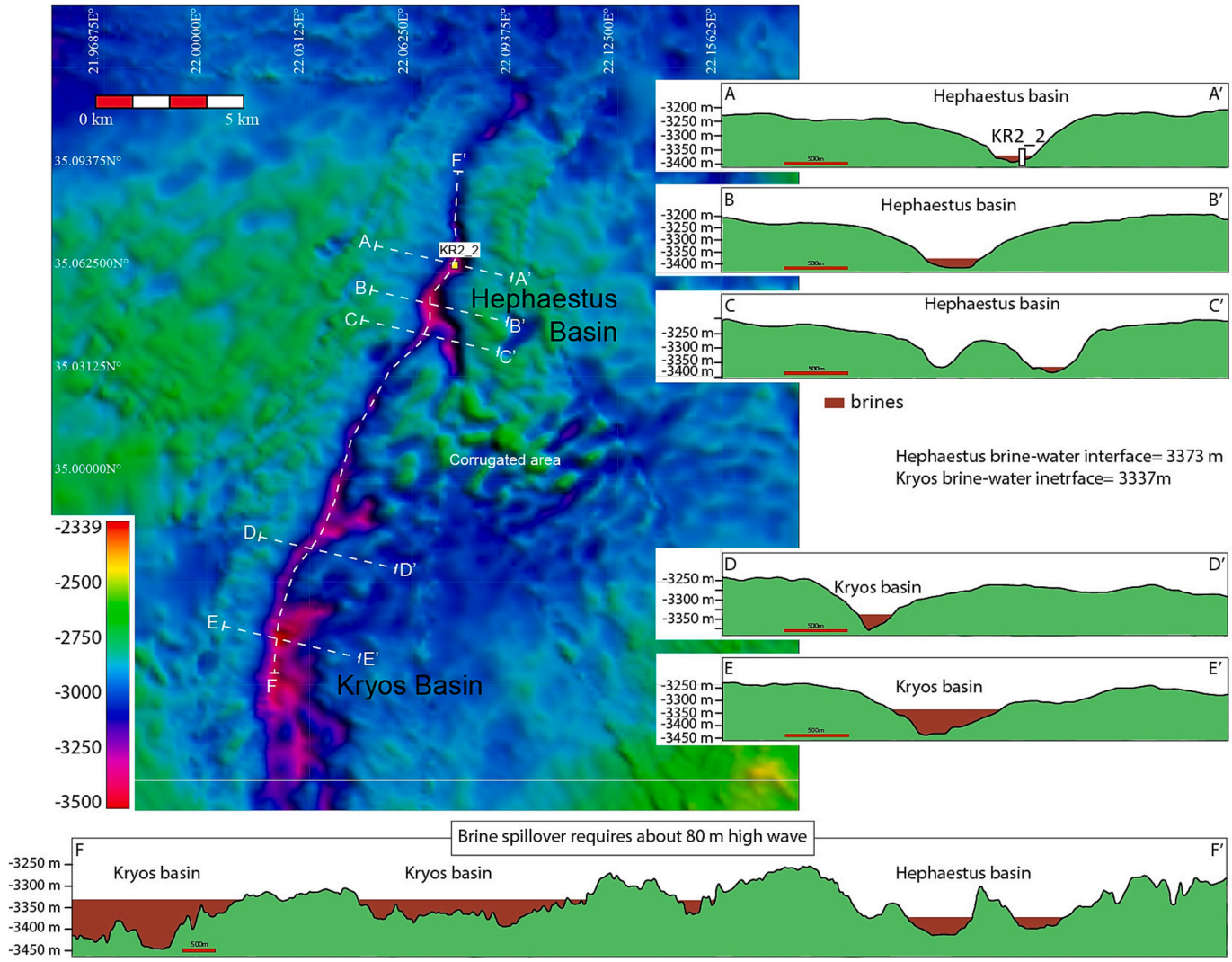

Fig. 2. Multibeam map showing location and geometry of the Hephaestus and Kryos anoxic basins. Location of the gravity core KR2_2 is indicated by a yellow square. A, B, C, D, E, F: cross-sections across the Kryos and Hephaestus anoxic basins. (For interpretation of the references to color in this figure legend, the reader is referred to the web version of this article.)

5.2. Core lithology based on grain size, XRF, MS and CT data

Core KR2_2 reveals five distinct sediment units, each characterized by different colors, lithology and internal structure (Fig. 4).

Unit A (250–298 cm): the deepest part of the core comprises laminated muddy silt high in Ca. It is interrupted by two coarser very dark sandy silt layers rich in S, Ba, Br and Mo.

Unit B (233–250 cm): it consists of laminated muddy silt, showing enrichment in detrital elements (Al, Zr, Fe, Ti) at its base.

Unit C (90–233 cm): it is characterized by deformed and convoluted silty sediment with varying colors and texture. It appears as a stack of sediment packets whose size decreases upwards. Sediment deformation intensifies in the uppermost levels that show a slightly coarser grain size and higher values of MS. The chaotic and convoluted sediment packets contain dark lenses high in OC, C/N, Ba and S at depth of 170, 117, 112 and 95 cm (brown layers in Fig. 4). CT scans of the upper part of this unit shows the presence of centimetric highly reflective patches corresponding to gypsum crystals (Section 5.5).

Unit D (25–90 cm): a 35 cm thick sandy silt unit with a basal coarse reverse graded sandy interval (D1 in Fig. 4) characterized by two sand inputs each marked by distinct peaks in Md (Fig. 4). Black patches in the chaotic fabric of the basal part (brown layer at 85 cm, Fig. 4) are associated with geochemical anomalies (high Ba, S, Br, Mo, OC, C/N). The intermediate sub-unit D2 (Fig. 4) is rather homogeneous while the upper D3 sub- unit shows an increase in Fe and S elemental trends and CT scans reveal cm-size gypsum crystals (Section 5.5).

Unit E (0–25 cm): it is represented by black and viscous muddy silt. The upper 20 cm (E2 in Fig. 4) lacks internal structures and shows centimetric, high reflective patches in the CT scans (Unit E2 in Fig. 4) while the lowermost 5 cm show internal layering (E1 in Fig. 4). These two units are marked by differences in geochemical data with an increasing trend in S towards the top.

5.3. Organic carbon, nitrogen and biomarkers

The analysis of lignin phenols and cutin acids within the sediment core revealed intricate patterns exhibiting non-correlated downcore variability (Fig. 5), which is uncommon in modern marine settings where individual terrestrial biomarkers (i.e., cutin-derived products and lignin monomers) are typically well-coupled. Rather than serving as a stratigraphically resolved record of terrestrial organic carbon (TerrOC) deposition, these biomarkers are used here primarily to rule out or constrain specific processes, such as input from riverine sources or reworking from shallow environments.

Lignin concentrations varied within individual sedimentary units, ranging from 1.09 mg/g OC in unit C to 0.04 mg/g OC in unit C,

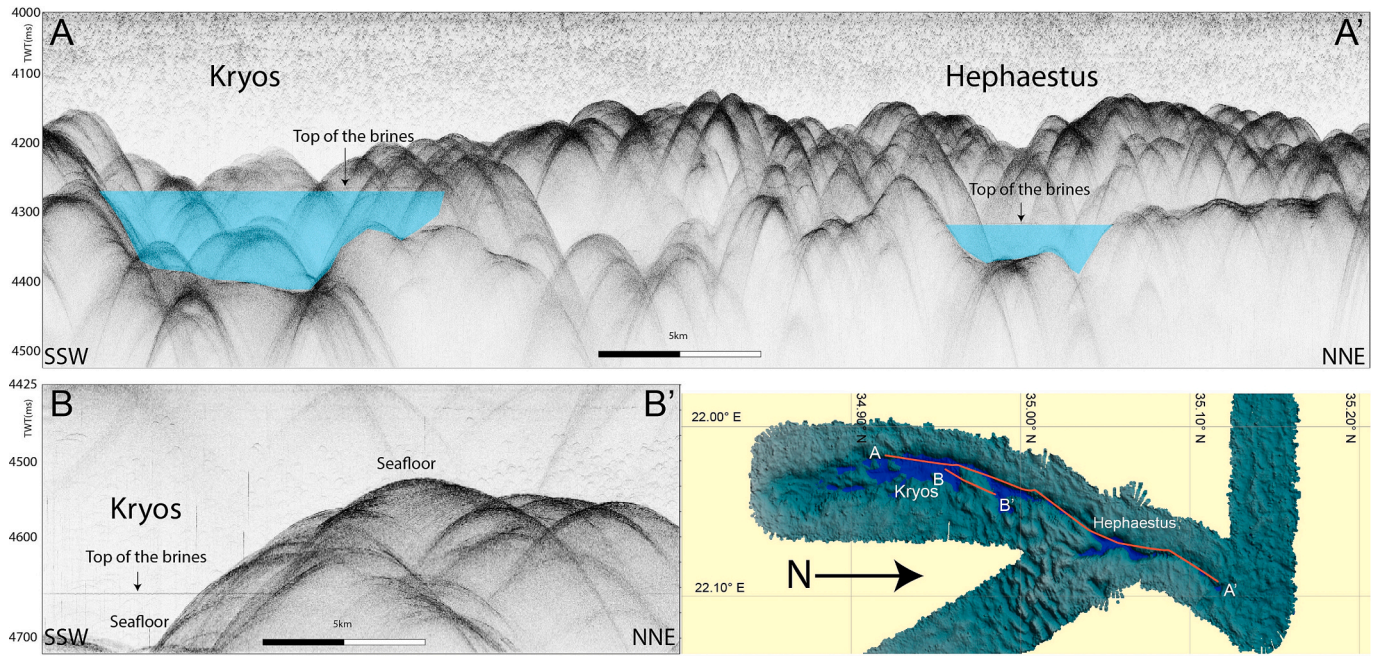

Fig. 3. Chirp profile across the Kryos and Hephaestus basins. A-A' Chirp profile along the two basin axis and the intervening structural high. B-B': Chirp seismic profile across the Kryos basin. The top of the brines is represented by the sharp reflector between normal seawater and dense brines. Location of seismic reflection profiles is shown in the map (lower right panel) where the extension of the brines in the two basins is shown in blue. (For interpretation of the references to color in this figure legend, the reader is referred to the web version of this article.)

showcasing variability even within the same unit. Overall, lignin phenols exhibited a distinct distribution pattern, with higher concentrations typically observed in the lower part of the core, particularly in Units A and C. Notably, the highest concentrations of cutin acids were observed in Units B (0.76 mg/g OC) and A (0.65 mg/g OC). It is important to note that due to OC normalization, the data primarily reflect the dominant organic matter source. However, given their extremely low OC content (SM6), Units B and A likely represent highly degraded environments where the more refractory, terrestrial organic matter has become selectively concentrated. Consequently, these units should not be interpreted as evidence of enhanced land-to-ocean exchange but rather as products of early post-depositional diagenesis. Furthermore, elevated levels of cutin acids were also detected in the upper anoxia units E2 and E1, averaging around 0.5 mg/g OC. The relatively high values of lignin and cutin biomarkers in the upper Unit E might be somehow due to relatively younger age and, thus, less degraded organic matter due to anoxic water.

The upper Unit E (sample E1) that shows an oily-like texture which could potentially indicate fluid escape of thermally mature organic matter was further characterized using the *n*-alkanes fingerprint (SM2) to distinguish fresh plant material from thermally mature oil. To distinguish biospheric vs thermogenic sources, we used the CPI index (CPI 7.6) which indicates poorly altered terrestrial material and, thus, it rules out the presence of oil fluids. In addition, the chromatograph exhibits a large peak in sulfur further highlighting the anoxic environment driven by the brine-rich bottom waters.

5.4. Foraminifera

5.4.1. Planktic foraminifera

The uppermost subsamples contain mainly gypsum, while foraminifera are absent. Conversely, the planktic foraminifera in the lowermost part of the core (Units A and B) are very abundant and generally well preserved (Fig. 6). Twenty taxa belonging to planktic foraminifera were recognised in the examined samples, and their distribution is reported in SM3. The interval between core bottom and cm 276 shows abundance of warm water taxa (*Globigerinoides ruber* followed by *Globoturborotalita rubescens* and *Globigerinoides sacculifer*) and presence of *Globorotalia inflata*. At 273 cm Neogloboquadrinids (first *N. incompta* followed by *N. dutertrei*) increase abruptly. Concurrently, a peak of *Globorotalia truncatulinoides* left coiling is recorded at 271.5 cm. Upward, warm water taxa show a progressive decreasing trend culminating at 254.5 cm, where they are near-absent, and the assemblage is dominated by Neogloboquadrinids, *Turborotalita quinqueloba* and *Globigerina bulloides* with *Globorotalia scitula* and *Globigerinita glutinata*. The samples 271–272/272–273 cm and 254–255 cm of core KR02_2 include planktic foraminifera specimens with thin tests frequently "smeared" by pyrite and with inflated chambers (increase in test size), these later in particular in *G. ruber* pink variety and *Orbulina*. In these samples *G. inflata* is near-absent. Fragmented tests were common in sample 271–272 cm.

5.4.2. Benthic foraminifera

Benthic foraminiferal assemblages are composed by a total of fifty-three taxa with variable occurrence in the different sediment units (Fig. 7).

Unit E is characterized by sediment totally barren in benthic foraminifera.

Unit D is characterized by distinct layers some totally barren in benthic foraminifera (D2 and D3 and the dark patch at 85 cm), others (D1) showing taxa common of bathyal domains (*Articulina tubulosa*) as well as displaced foraminifera from neritic environment (*Pyrgo depressa* and *Quinqueloculina padana*) (Fig. 7).

The interval between 88.5 and 112 cm (top of Unit C) is characterized by significant increase in weight fraction > 125 μ due to the presence of gypsum crystals. In the dark lenses at 112 and 170 cm benthic foraminifera are absent whereas in the immediately pre- and post-dark lenses, the species *A. tubulosa* dominates the assemblage. The unit includes species displaced from neritic environment (e.g., *Angulogerina angulosa* and *Quinqueloculina padana*; Fig. 7).

Unit B is characterized by relatively high values of diversity and density and includes benthic foraminifera from abyssal domain (*A. tubulosa*) together with genera from neritic environment (*Ammonia*,

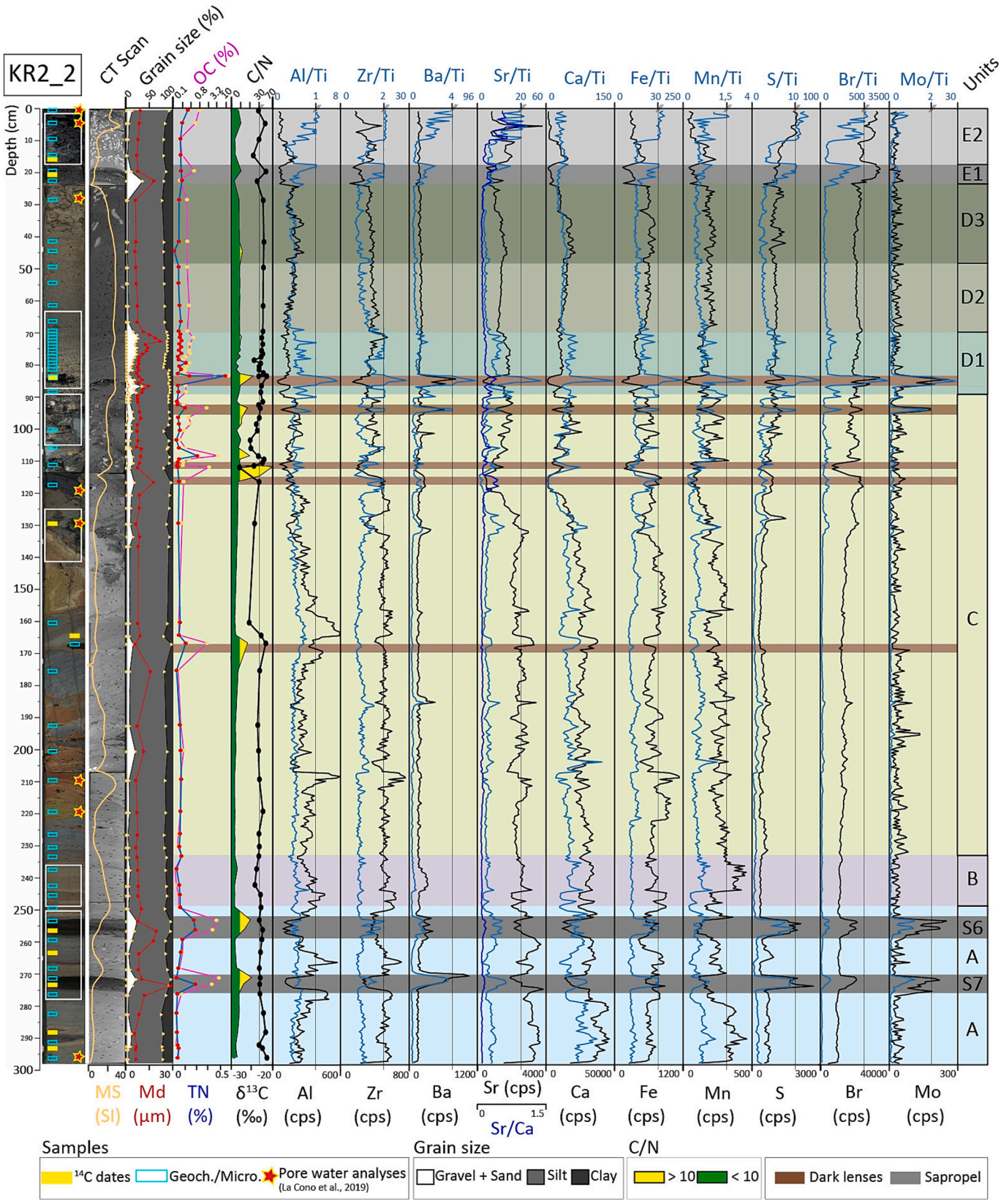

Fig. 4. Log of core KR2_2. From left to right: photograph with analysed sediment samples; computed tomography (CT) scan with magnetic susceptibility (MS) in yellow; grain size % with mean diameter (Md) in red; XRF data plot along the study sample; subdivision in individual sediment units (for more details Table 2). Yellow rectangles on the core photograph represents ^{14}C dated samples in Table 1. S6, S7: sapropel S6 and S7. Red stars: samples used for PW analyses. (For interpretation of the references to color in this figure legend, the reader is referred to the web version of this article.)

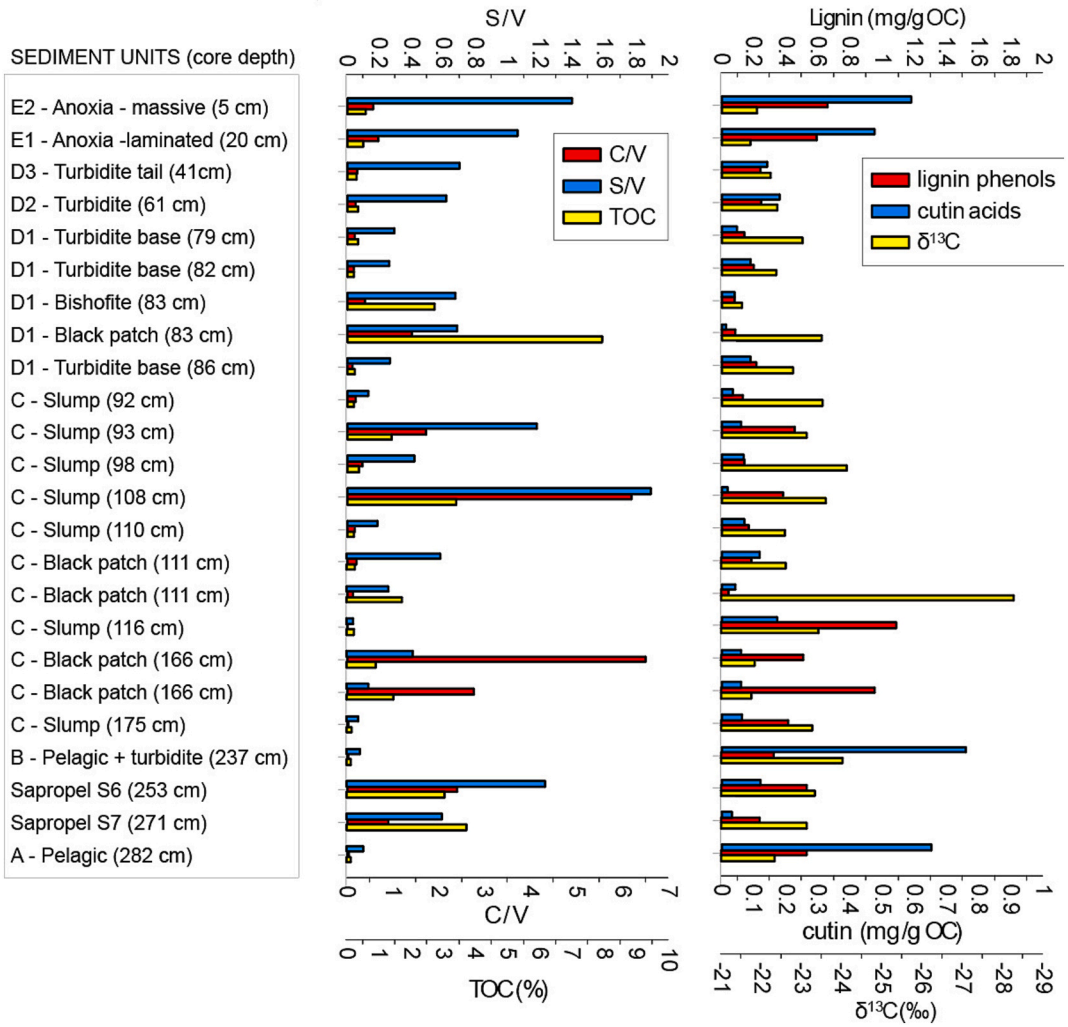

Fig. 5. Bulk properties and lignin phenol fingerprint in different units of the sediment core. a) Total organic carbon (TOC, %), syringyl/vanillyl (S/V) and cinnamyl/vanillyl (C/V) ratios; b) stable carbon isotopes ($\delta^{13}C$, ‰), lignin content (mg/g OC), cutin acids (mg/g OC).

Quinqueloculina and *Triloculina*) (Fig. 7).

The lowermost part of the core (Unit A) is characterized by the dominance of *A. tubulosa* with very low species diversity and density (Fig. 7); benthic foraminifera are absent in the two dark layers within Unit A.

5.5. Mineralogical analysis

Mineralogical association varies throughout the core (SM7).

In Units A and B the detrital component is very low and mainly represented by mica and pyrite.

Unit C is characterized by a larger component of minerals. The detrital component is mainly represented by magnesite, Mg-calcite, clay minerals, quartz, mica (muscovite and biotite), kaolinite, dolomite, halite and patches of bishofite, pyrite, iron hydroxides and gypsum.

The mineralogical association of Unit D includes micas, clay minerals, crystal clusters of gypsum (including desert rose crystals), quartz, kaolinite, feldspar (albite) and mineral grains rich in Mg.

The topmost unit E shows very abundant gypsum crystals with different morphologies (including desert rose crystals, blocky crystals, discoidal crystals).

5.6. Radiometric dating

Table 2 summarizes results of radiometric dating. ^{14}C dating of planktic foraminifera in the basal part of core KR2_2 has provided uncalibrated ages of 38000 ± 600 BP, 48000 ± 3000 BP or older, while the age of the OC black patch at 84 cm depth within the turbidite is 7850 ± 50 BP and 47000 ± 3000 BP (not calibrated). The uppermost dated samples are located at the base of the anoxic sediment (17 and 21 cm below the core top) and the dated sediment bulk OC provides an age of 2005 ± 30 BP and 2700 ± 30 BP (not calibrated).

6. Data interpretation

6.1. Chronology

The samples from dark layers within Unit A (intervals 254–255 and 271–273 cm) show a foraminiferal feature typical of sapropel deposition (Narcisco et al., 2012 and references therein) as confirmed also by the dark brown-black sediments, high OC content, peaks of Ba and Mo (Fig. 6). The planktic foraminifera assemblages reported in literature for the late Quaternary sapropels deposited in Eastern Mediterranean, have been described not only in terms of taxa and their distribution, but also regarding some aspects of the test morphology. In addition to the pyrite frequently present within the tests, sapropels deposited during warm climate intervals (such as Sapropels 1, 5, 7) show the taxon *Globigerinoides ruber* pink variety with thinner test, strongly inflated chambers and large secondary apertures (Negri et al.,1999 and references therein, Narciso et al., 2012). Similar test features affect other taxa such as

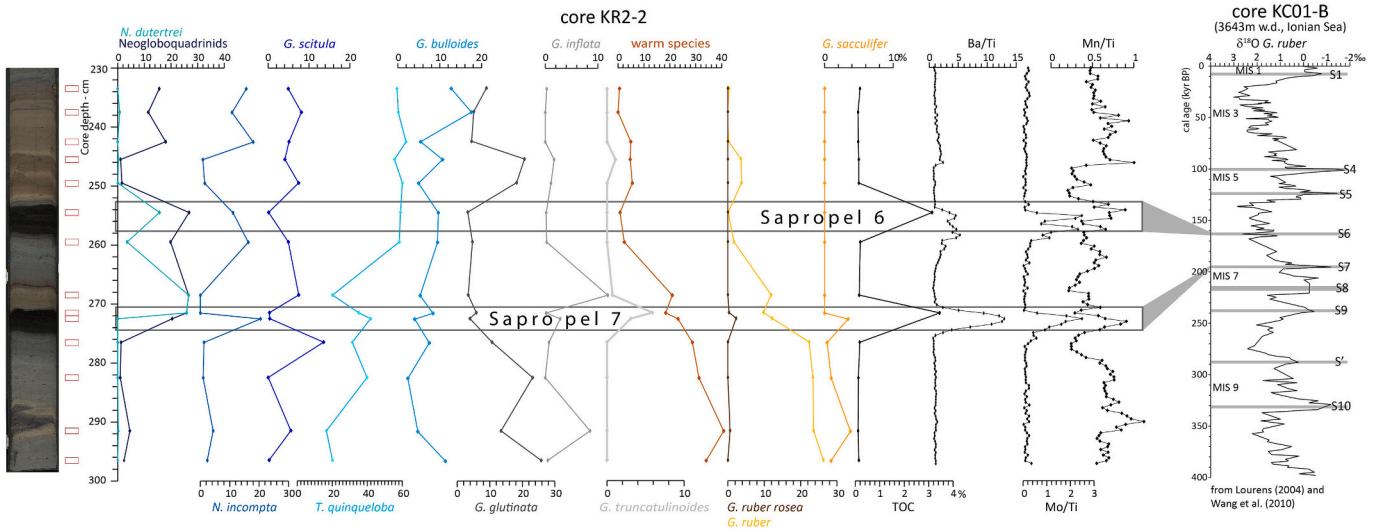

Fig. 6. Distribution of planktic foraminifera in the lower part of the core along with OC and productivity (Ba) and redox sensitive elements (Mo and Mn). The record of these later mark the sapropel deposits with abrupt and positive peaks. Mo/Ti and Mn/Ti peaks also correspond to the negative peaks (absence) of the benthic foraminifer A. tubulosa (see Fig. 7), a taxon not tolerating low oxygen/high accumulation of organic matter (Jorissen, 1999). Warm taxa include G. ruber (pink and white varieties), Beella digitata, Globigerina calida, G. rubescens, Globigerinoides tenellus, Globigerinella siphonifera, G. sacculifer (including G. trilobus and G. quadrilobatus), Orbulina suturalis, Orbulina universa. The red rectangles are the studied samples, while the rectangles indicate the sapropels. The stratigraphic position of the Sapropels occurring during the late Quaternary in the reference core KC01-B is also reported on the right. (For interpretation of the references to color in this figure legend, the reader is referred to the web version of this article.)

Orbulina, Globigerinoides sacculifer and Globigerina bulloides, with large-size and thin-walled tests (Negri et al., 1999). The reasons of these morphological features have been interpreted as the response of surface dwelling taxa to the decrease of surface water density because of the salinity decrease (Negri et al., 1999) to improve the test buoyancy. Another microfaunal characteristic of sapropels of the Eastern Mediterraneanis is the high abundance of dextral-coiled Neogloboquadrinids, in particular the taxon *N. dutertrei* (Cita et al., 1977).

The two sapropel intervals (252–258 cm and 270–276 cm) indicate two different oceanographic conditions. The lower interval suggests warm and stratified waters, characterized by a Deep Chlorophyll Maximum development (abundant Neogloboquadrinids) and strongly oligotrophic surface waters (*G. ruber*, *Orbulina*, *G. sacculifer*, *G. rubescens*) (Fig. 8). Deep Chlorophyll Maximum (DCM) occurs when upper water column stratifies and the chlorophyll, produced by plants/phytoplankton, reaches the maximum concentration at a water depth with the pycnocline positioned close to the base of the euphotic zone. The maximum depth is regulated by the minimum light intensity necessary for the growth of phytoplankton. DCM is present only in the areas where the pycnocline is situated at depths above or near the light compensation depth (Fairbanks and Wiebe, 1980; Rohling and Gieskes, 1989). On the other hand, the upper sapropel interval suggests cold, productive and stratified waters (lack of warm taxa and abundance of Neogloboquadrinids and *T. quinqueloba;* i.e., glacial sapropel). These environmental observations may contribute to the chronology assessment of the core. Neogloboquadrinids are present in the sapropels deposited in the Eastern Mediterranean except for Sapropel 1 (Rohling et al., 2015 and references therein). Therefore, the oldest sapropel (270–276 cm) cannot be considered younger than Sapropel 5 (128.3–121.5 ka according to Grant et al., 2016), which is the youngest sapropel with Neogloboquadrinids deposited during warm climate conditions. Nevertheless, the presence of *G. truncatulinoides* in the upper part of the older sapropel suggests instead Sapropel 7 (195 ka according to Lourens, 2004) as minimum age, as this taxon has not been recorded in literature within Sapropel 5, while it is present in Sapropel 7 deposited during warm climate condition (Capotondi et al., 2016 and references therein). Radiocarbon dating obtained within and close to these two intervals all indicate ages beyond the radiocarbon time range limit (55000 calibrated yr BP). This supports the chronology inferred by the microfaunal content and related to the known sapropel stratigraphy.

Within Unit C, radiometric dating provides uncalibrated ages between 48 and 38 ka BP, while very different uncalibrated ages of 7850 ± 50 BP and 47000 ± 3000 BP obtained from the sediment bulk OC characterize the basal part of Unit D1 (Fig. 4 and Table 2). In the uppermost part of the core, the radiocarbon ages at 17 cm and 21 cm (Unit E1, 2700 ± 30 BP and Unit E2, 2005 ± 30 ^{14}C yr BP respectively) were obtained from the sediment bulk OC, due to the absence of foraminifera and of any other calcareous remain. In Table 2 we report also calibrated radiometric ages (2σ) using ΔR = 0 performed with Calib software (CALIB rev. 8; Stuiver and Reimer, 1993) using the Marine20 calibration curve. Based on these results, the basal part of Unit E1 was deposited in the time window Cal BCE 416-Cal CE 112 while the basal part of unit E2 was deposited in the time window Cal CE 418–673.

6.2. Sediment facies

The sediment core records sedimentation during the last ~200 kyr and includes pelagic intervals, sapropelitic sediment, slump deposits, chaotic layers, a thick turbidite bed and a very recent anoxic and viscous sediment unit.

Background marine conditions are represented by high-Ca content pelagic intervals (Unit A) at the base of the core (Table 3 and Figs. 4 and 8). Within this unit benthic foraminiferal assemblage is dominated by the abyssal taxa *A. tubulosa* (Fig. 6) that is common in deep-water Mediterranean Quaternary pelagic sediment (De Rijk et al., 1999; Jorissen, 1999; Mullineaux and Lohmann, 1981; Polonia et al., 2023; Sgarrella and Moncharmont Zei, 1993). Two layers of sapropelitic sediment interrupt pelagic sedimentation and are interpreted as Sapropel 7 (S7) and Sapropel 6 (S6) based on their micropaleontological association (Table 3).

Unit B still includes taxa common of the bathyal domain (*A. tubulosa*) together with displaced foraminiferal assemblage from neritic environment (Fig. 6), suggesting it might represent deep sea sediment including fine turbidite beds.

The highly deformed and convoluted clayey silt Unit C is a 135 cm thick slump represented by a stack of sediment characterized by

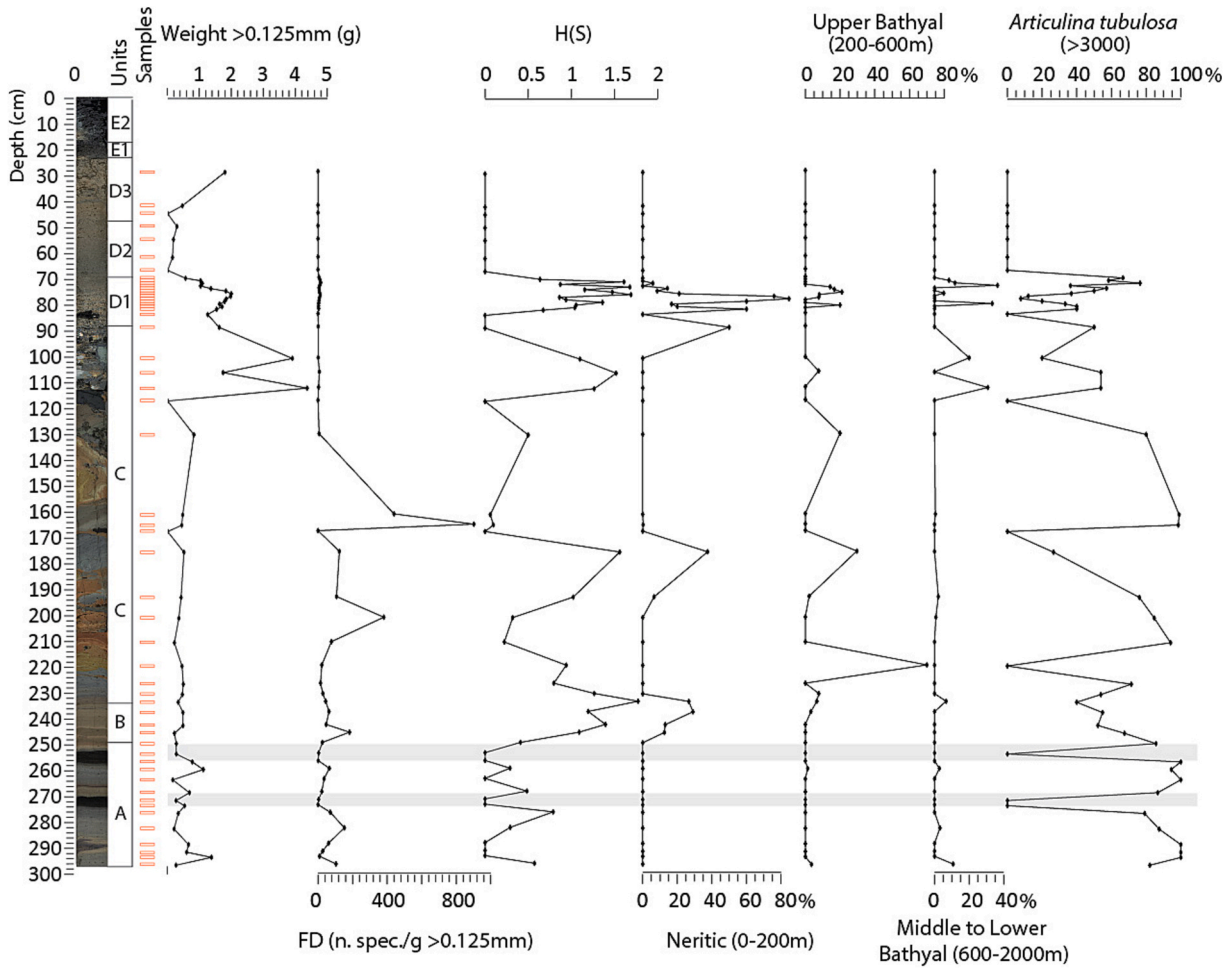

Fig. 7. Weight (g) of the fraction > 0.125 mm. Benthic foraminiferal density (FD) is expressed as number of specimens per dry gram of sample fraction examined. Species richness H(S) is the species count in a sample or an aliquot. The relative abundance of 3 groups distinguished by their habitat preferences was calculated to demonstrate their distribution in the samples. Species used to compile data for each depth classes are listed in Supplementary Material SM4.

different lithology, geochemistry and provenance. Grains size of the gray, yellow and brown-colored intervals span from silt to sand. Visually prominent because of their color and structure variations, these intervals have been sourced from different bathymetric ranges. Deep water benthic taxa prevail together with co-occurrence of neritic and upper bathyal species, but inner and outer shelf material is also present. The black patches within Unit C (Figs. 4 and 8) show very different composition compatible with evaporitic material (bishofite, halite, gypsum, rock salt, pyrite, Mg-carbonate). Other gelatinous pellicles associated with anoxic sediment were described in other deep sea brine lakes (Erba et al., 1987a; Erba et al., 1987b). The Ca content is rather constant throughout this unit, and similar to those of the pelagic units, suggesting remobilization of surficial slope pelagic sediment. We interpret this unit as related to re-sedimentation processes affecting deep water sediment, including brine-related evaporites and inputs from inner and outer shelf.

The slumped Unit C is covered by a 65 cm thick turbidite bed (Unit D) with multiple sand pulses, stacked units with reverse grading and a very fine and homogenous upper part with gypsum crystals interpreted as the homogenite part of the turbidite (Polonia et al., 2017) (Units D2 and D3 in Figs. 4 and 8). The sand content in the basal part of Unit D1 is the highest recognized throughout the core (30–40 %). The turbidite is characterized by an upward decrease in benthic foraminiferal density and a progressive increase in diversity mainly due to the presence of taxa displaced from the shelf areas that take on frequencies of over 32 % (Fig. 7). At the base of the turbidite the very dark sediment patch at 85 cm showing an OC content up to 7 % is interpreted as bischofite based on mineralogical analysis (SM7) with gypsum and pyrite entrained from another brine lake or from fossil evaporites.

The turbidite bed is capped by very dark and viscous muddy silt unit (Unit E) barren of foraminifera and biogenic material. The basal sub-unit E1 shows sub-horizontal laminations while the upper sub-unit E2 is homogeneous with abundant high-reflective crystals of gypsum (Fig. 4). This Unit is interpreted as anoxic sediment within a brine lake. Basal laminations in sub-Unit E1 might be related to confined basin seiche following the deposition of remobilized material as suggested for tsunamigenic seismo-turbidites (Polonia et al., 2017, 2022).

Lignin phenols and cutin acids trends are indicative of a complex terrestrial input within the different sediment units, alongside changing redox conditions and primary productivity. While the presence of terrestrial-derived material is evident, lignin phenols and cutin acids do not exhibit the expected linear relationship with stable carbon isotopes, with high biomarker values usually associated with depleted isotopic composition. This further underscores the complexity of the stratigraphic units, the presence of multiple reworked sources and suggests nuanced interactions between terrestrial and marine processes shaping the sedimentary record. These patterns, which do not resemble those usually observed in river-dominated margins (e.g, Tesi et al., 2007), suggest the involvement of diverse processes in organic matter deposition and preservation. Yet, considering the overall concentration of lignin and cutin acids, we can surely exclude a direct input from local rivers (i.e., flood events) or inner-shelf regions while, most likely, the

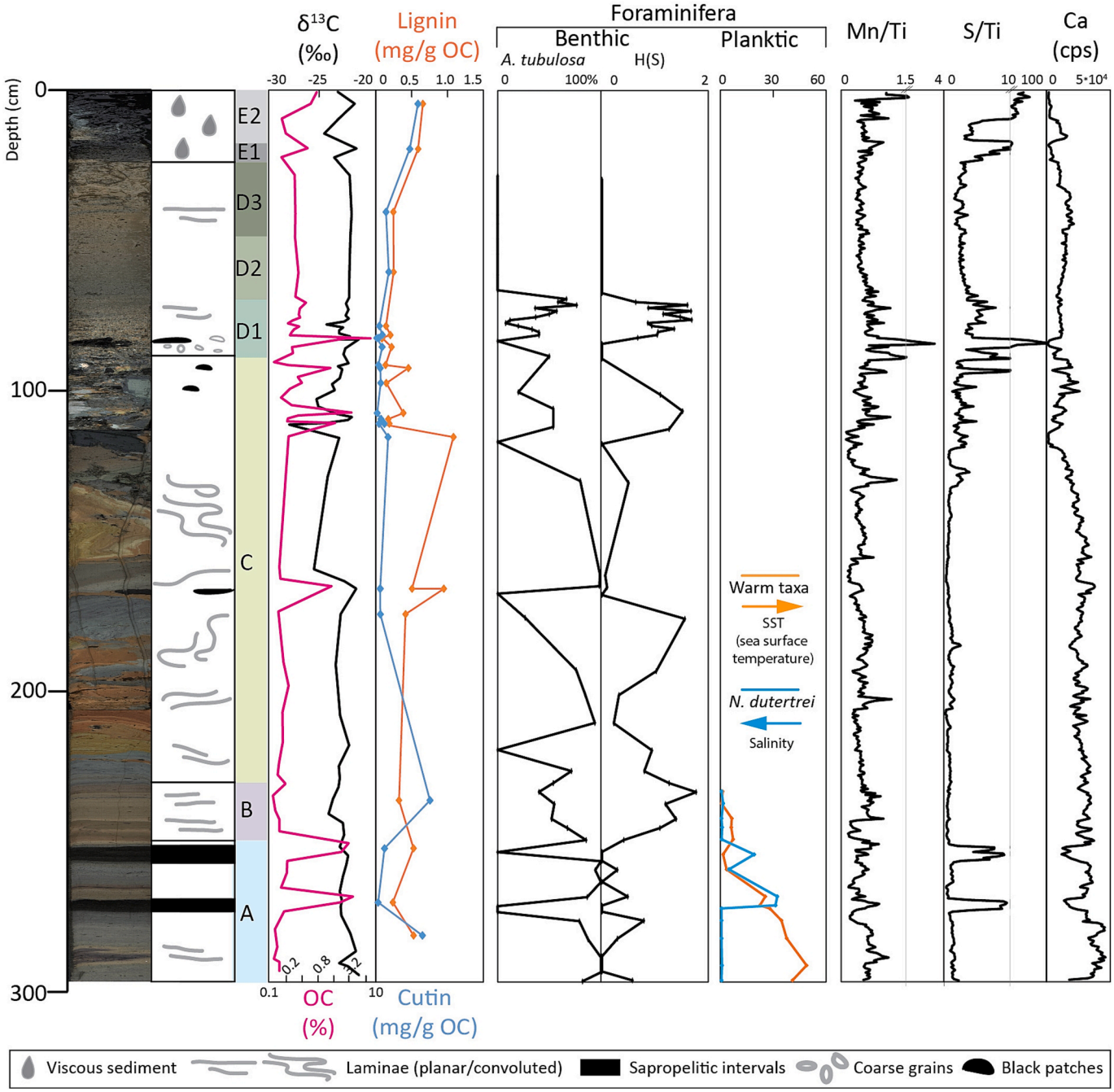

Fig. 8. Composite stratigraphic plots showing from left to wright: core photograph, facies interpretation and sediment units; $\delta^{13}C$ (‰); lignin content (mg/g OC) and cutin acids (mg/g OC); benthic foraminifera trends: *A. tubulosa* indicative of deep water (>3000 m) environments and Species richness H(S); planktic foraminifera: warm taxa (orange), positively correlated with sea surface temperature, and *N. dutertrei* (blue), negatively correlated with salinity; XRF data major elemental plots (Mn/Ti, S/Ti, Ca) along the sediment units. (For interpretation of the references to color in this figure legend, the reader is referred to the web version of this article.)

observed terrigenous-poor concentrations reflect a long-range transport of land-derived material prior to deposition. In addition, by coupling together $\delta^{13}C$ and biomarkers we can further refine the interpretation of the depleted stable carbon isotopic composition, in particular those depleted values that could be indicative of river influence (Figs. 4 and 5) exhibit low concentrations of terrestrial biomarkers, likely indicating the presence of thermally mature organic material like shale (i.e., black patches within Units C and D).

6.3. Turbidite emplacement time based on age modeling

Since the dated samples are not located directly at the top of the turbidite, we reconstructed the sedimentation rate from the anoxic sequence (from the core top to the uppermost dated sample) to interpolate the age of the turbidite. The dated samples were collected 1 cm above the base of Unit E2 and within the laminated unit E1. Given that the laminated unit E1 might be related to seiching processes occurring immediately after the catastrophic event – potentially entraining older material during sediment transport – we consider the uppermost dated sample to provide the most reliable radiometric age for estimating the timing of turbidite emplacement. The interpolated age of the turbidite, therefore, should be adjusted by the time corresponding to 1 cm of sediment accumulation below the dated sample.

To estimate the pelagic sedimentation rate within the anoxic basin,

Table 3
Summary of sediment facies. Column A: sediment unit. Column B: photograph of the different sediment units with radiometric dating results in yellow. Column C: sediment color. Columns D and E: micropaleontological, geochemical and mineralogical characteristics of the different sediment units. Column F: facies interpretation.

E 2500±30 yr 2700±30 yr	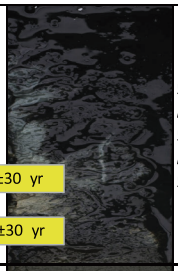	5Y 2,5/2 *black*, 5YR 5/3 *reddish brown*, 2,5Y 5/1 *gray*	Very dark and oleos clayey silt with coarser (sandy silt) interval in its basal section		Anoxic sediment from brine lake
			Planktic foram.	Barren	
			Benthic foram.	Barren	
			Mineralogy	Gypsum (large crystals and "desert rose" aggregates), oxidized pyrite, iron hydroxides crusts.	
			Geoch.	S, Fe, Mn, Ba, Al	
				Corg < 0.76%	
				-21,73‰ > δ13C > -24,85‰; C/N: 2.7-10.2	
D 7850±50 yr 47±3 kyr		5Y 5/2 *grayish brown, 5Y 2,5/2 black patches*	Clayey silt with reverse-graded, sandy-silty sub-unit in the basal section (D1)		**Basal part:** turbidite with dominant inner shelf speies; **Middle part:** turbidite with dominent abyssal speies; **Upper part** (from sample 48 to the top) barren: homogenite part of the turbidite
			Planktic foram.	Upper part: absent, basal part: abundant of mixed environment (warm and oligotrophic plus cold and productive taxa)	
			Benthic foram.	**Basal part**: abundant abyssal taxa (Articulina tubulosa) and displaced neritic taxa (Quinqueloculina auberiana, Quinquloculina padana)	
			Mineralogy	Gypsum (large crystals, discoidal grains, "desert rose" aggregates), oxidized pirite, iron hydroxides crusts, magnesite, Mg-calcite, clay minerals, bischofite.	
			Geoch.	Variable geoch., see figure 3	
				Corg < 0.5%; 34bis: 2,7-7,9 %.	
				-21,5‰ > δ13C > -24,66‰; C/N: 4.1-11; **34bis**: 20.7-23.9.	
C 38±0,6 kyr	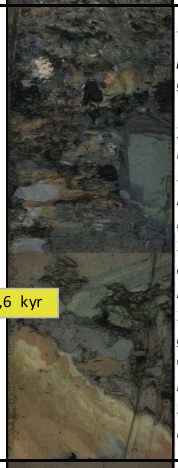	7,5YR 6/2 *pinkish gray*, 10YR 5/6 *yellowish brown*, 5YR 4/4 *reddish brown*, 2.5Y 4/3 *olive brown*, 2.5Y 5/1 *gray*, GLEY 2 4/1 *bluish gray*, 5Y 2.5/2 *black*	Highly deformed and convoluted clayey silt; the sand fraction locally prevails over clay, often in correspondence of black patches; stack of different sediment packets.		**Basal part:** local remobilization of pelagic sediment; **Middle part:** outer and inner shelf material; **Upper part:** upper slope and brines (samples 26 e 31). **The slump includes sapropel sediments and brines.**
			Planktic foram.	**Upper part:** scattered samples with planktic forams absent (93.5 and 98.25), and representative of sapropel deposition in warm water (not S1) (96.5) and cold water environment (97.5), warm water conditions (103.5) and reworked microfauna (109.5). **Middle part:** forams near-absent in a possible turbidite tail deposition (169)	
			Benthic foram.	**Basal part:** A. tubulosa (lower abyssal) and upper bathyal taxa (Pyrgo depressa) bathyal taxa; **Middle part:** neritic species (Angulogerina angulosa and Quinqueloculina padana); **Upper part:** A. tubulosa (lower abyssal)	
			Mineralogy	Magnesite, Mg-calcite, clay minerals, pyrite, micas.	
			Geoch.	Variable geoch., see figure 3	
				Corg < 0.4 %; black patch with Corg = 3,41%.	
				-21,74‰ > δ13C > -28,26‰; C/N: 3.2-70.	
B		5YR 4/4 and 5/3 *reddish brown*	Faintly laminated clayey silt.		Slumped/remobilized material of local and coastal origin.
			Planktic foram.	Cold-temperate assemblage of productive waters	
			Benthic foram.	*A. tubulosa* (lower abyssal) and genera from neritic environment *(Ammonia, Quinqueloculina and Triloculina)*	
			Mineralogy	Micas (muscovite and biotite)	
			Geoch.	Al, Zr, Sr, Ca, Fe, Mn	
				Corg < 0.15 %	
				-22,93‰ > δ^{13}C > -24,43‰; C/N: 3,2-6,3	
A > 53 ky > 49 ky > 47 ky	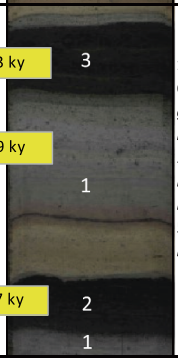	**1)** 7,5YR 6/2 *pinkish gray*, 5/2 *brown* and 5YR 5/3 *reddish brown*; **2/3)** 5Y 2,5/2 *black*	**1:** laminated clayey silt; **2/3:** massive, structurless sandy silt.		**1:** Pelagic sediment; **2:** Sapropel S7; **3:** Sapropel S6
			Planktic foram.	**1:** warm water taxa with a general decreasing trend upward, **2**: assemblage suggesting sapropel deposition in warm water, **3**: assemblage suggesting sapropel deposition in cold water	
			Benthic foram.	**1:** *A. tubulosa* (lower abyssal); **2/3:** barren	
			Mineralogy	**1:** pyrite and terrigenous grains; **2/3:** pyrite	
			Geoch.	**1:** high Ca; **2/3:** high Ba, S	
				1: Corg < 0.3 %; **2/3:** Corg 2-3.7	
				1: -21.48‰ > δ^{13}C > -23.42‰; C/N<10; **2/3:** -22.52‰ > δ13C > -23.33‰; C/N > 10.	

we assumed that the top of the core corresponds to the seafloor in 2015, when the sample was collected, and used the calibrated radiocarbon age of the sample at 17 cm depth (CE 418–673, assuming $\Delta R = 0$). Based on these data, the average recent sedimentation rate in the anoxic Hephaestus basin is estimated at 0.115 mm/yr (0.10–0.13 mm/yr). This value is consistent with sedimentation rates between 0.05 and 0.3 mm/yr previously reported by Cita et al. (1998). This implies that, under normal pelagic conditions, 1 cm thick sample used for radiometric dating represents an integrated time span of approximately 79–94 years. Therefore, dating a sample located 1 cm above the turbidite introduces a corresponding age offset, which must be taken into account when estimating the timing of the turbidite emplacement. This results in an estimated deposition window for the turbidite of approximately CE 324–594. This age estimate is subject to uncertainties inherent to the radiocarbon dating process including possible sample contamination, the presence of reworked (older) organic carbon, ΔR, and reservoir effects. However, uncertainties related to bioturbation are considered negligible in the anoxic conditions of the Hephaestus basin.

The turbidite age derived from interpolation has been further refined through OxCal age modelling (Bronk Ramsey, 2008). We constructed a deposition model for the uppermost part of the core by incorporating information on sediment stratigraphy and depth. Once the radiocarbon dating information was introduced into the model (Fig. 9) the pelagic sedimentation rate was derived from the modelled time-depth curve for the dated pelagic sediments. The software finds mathematically a representative set of possible ages for each depth point in a sedimentary sequence and turbidite age distribution at 2σ is modelled from its stratigraphic depth of emplacement into the background sequence (Fig. 9). The time-window for turbidite deposition derived through Oxcal age modelling is CE 155-439 (Fig. 9). The age intervals derived from the OxCal modelling incorporates various sources of uncertainties because it considers a random distribution of sedimentation and not constant as we did in the radiometric age analysis; moreover, each point is described by a probability density function, where the simple sedimentation rate corrections are not. This results in broader credible intervals that better reflect the inherent uncertainties in the dating data.

6.4. Sedimentary processes: Slump and turbidite triggering mechanism

Core KR2_2 intercepts the transition between "normal" deep water Mediterranean pelagic sediment and brine bearing anoxic sediment in the Hephaestus basin. The oxic-anoxic transition occurred after the emplacement of the ~2 m thick slump/turbidite deposit and, for this reason, seafloor anoxia appears related to the geological event that has triggered sediment instability. The slump and turbidite units are not separated by pelagic sediment and their composition, together with their gradual transition, suggest they might be related to a single mechanism capable of producing deep sea slope failures, entraining shallow water material from the coastal regions and transporting a complex mixture of shallow and deep-water sediment in the isolated basin. Based on age model results, such a catastrophic event occurred in the time window CE 155–439 (Fig. 9).

The transport of shallow water material and deposition of turbidites in the abyssal domain can be linked to a number of different triggering processes (Goldfinger et al., 2012) such as storms (Mulder and Alexander, 2001), sediment loading (Adams, 1990), hyperpicnal flow (Casalbore et al., 2011; Mulder et al., 2003), gas hydrate destabilization usually related to climate-driven instability (Rothwell et al., 1998), alteration of volcanic/hydrothermal deposits (Miramontes et al., 2018), great earthquakes (Goldfinger, 2011), tsunami (Kastens and Cita, 1981; Polonia et al., 2013; Polonia et al., 2021; Shanmugam, 2012).

Available data suggest that a storm or flood trigger is unlikely because in a similar abyssal oceanographic setting in the Ionian Sea recent major storms did not produced any sediment remobilization (Polonia et al.,2017). Flash floods have the potential to generate debris flows; however, such effects in the Mediterranean region have been

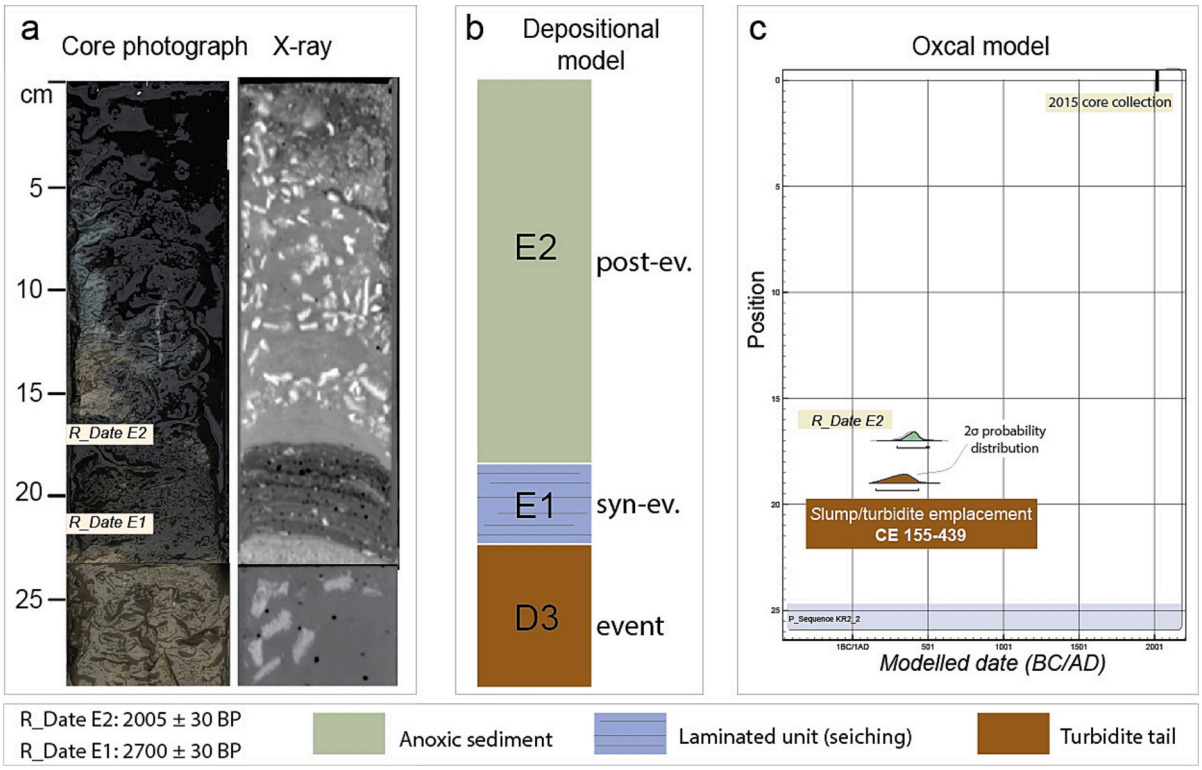

Fig. 9. Emplacement time window of the slump/turbidite as deduced through age modeling. a) Photograph and X-ray image of the upper part of the Kr2_2 core. d) depositional model as deduced through multi-proxy analysis of the gravity core. c) Age model results (OxCal v4.4.4 Bronk Ramsey, 2021; r:5 Marine09 marine curve, Reimer et al 2009). The turbidite/slump deposit was emplaced in the time window CE 155-439.

observed only in the shelf and upper slope environments (Casalbore et al., 2011; Polonia et al., 2017) and biomarkers within the resedimented deposit exclude a river-dominated source. Climate-driven slope instability is unlikely to be the triggering mechanism, given that radiometric dating indicates a time window for the slump and turbidite deposits that is not associated with significant climatic changes or sea level variations. Hydrothermal fluid expulsion is one of the most likely triggering mechanisms; however, analyses of sediment pore water suggest downward diffusion of brine from the surface into the sediments, rather than upward flow from deeper sources. Considering the thickness of the slumped material, we propose that a major earthquake and tsunami should be regarded as the most likely mechanisms responsible for triggering slope failures and sediment remobilization. This interpretation is supported by radiometric dating, which provides an emplacement time window for the slump and turbidite (CE 155–439) that closely aligns with the CE 365 earthquake and mega-tsunami known to have caused catastrophic effects in the Mediterranean Sea (Polonia et al., 2016).

The Hellenic Arc subduction system has produced strong ground shaking and uplifted paleo shorelines in Crete provide important information on timing and magnitude of large earthquakes in the forearc region (Pirazzoli et al., 1982; Tiberti et al., 2014; Mouslopoulou et al., 2015a; Mouslopoulou et al., 2015b). Based on historical descriptions and sedimentary records, the CE 365 Crete M > 8 earthquake impacted a broad geographical area and generated a *trans*-Mediterranean tsunami that triggered sediment remobilization for distances of 700–800 km from the source event (Bahrouni et al., 2024; Polonia et al., 2022; Salama et al., 2018). A more recent event, the M_w8 1303 CE earthquake (Papazachos, 1996), ruptured the eastern segment of the Hellenic Arc between Crete and Rhodes (Guidoboni and Comastri, 1997; Papadopoulos et al., 2007) and caused damage over a wide area. Other moderate to large earthquakes (M_w between 6 and 7.8) in the considered time window occurred in Syria, Lebanon or in Israel, but they did not affect Greece or Crete (Salamon et al., 2007). The only event capable of triggering resedimented deposits in the isolated Hephaestus basin is the CE 365 Crete earthquake and associated tsunami. This event is interpreted as the primary trigger for large-scale sediment remobilization prior to the onset of seafloor anoxia in the brine lake. Within this context, seismic shaking during the CE 365 event likely caused both the downslope displacement of sediment within the brine lake and the simultaneous generation of turbidity currents that transported shallow-water material from the coastal zone to the abyssal domain. Since the Hephaestus brine lake is disconnected from any canyon system, sediment transport likely occurred through unconfined, sheet-like processes rather than channelized flow. The texture and character of the sand lenses are comparable to those observed in abyssal seismo-turbidites (Polonia et al., 2021; Polonia et al., 2013), offshore tsunami deposits in the northernmost portion of the Gulf of Aqaba (Goodman Tchernov et al., 2016) and tsunamigenic turbidites in the Ionian abyssal plain (Polonia et al., 2022).

6.5. Isotopic analyses of brines

As mentioned in Introduction, most deep-sea hypersaline basins are thought to have arisen from the dissolution of subsurface evaporitic layer(s) after they were tectonically exposed to seawater (Cita, 2006). The brines of the Mg-saturated Discovery, Hephaestus and Kryos basins contain approx. 8 g kg^{-1} bromine (La Cono et al., 2019; Wallmann et al., 1997, 2002; Yakimov et al., 2015), a concentration typically found in bischofite, which precipitates in the final stage of brines when seawater is evaporated to a level of less than 0.5–1 % of its initial volume. Thus, the existence of the Discovery, Hephaestus and Kryos brines supports evidence that the Eastern Mediterranean basin evaporated almost to dryness during the Messinian salinity crisis (Cita, 2006; Wallmann et al., 1997).

Analysis of stable isotopes of $\delta^{18}O\text{-}H_2O$ and $\delta D\text{-}H_2O$ in brines provides information on the origin of these basins. We used this approach to analyze six Mediterranean deep-sea brines (L'Atalante, Discovery, Hephaestus, Kryos, Medee and Urania), bearing special attention to Mg-saturated basins. This scenario appears to apply to some, but not all, Mediterranean deep-sea brine pools. As shown in Fig. 10a, all analyzed brines can be divided in two principal groups: (i) brines with the $\delta^{18}O\text{-}H_2O$ / $\delta D\text{-}H_2O$ values similar to that of modern seawater (L'Atalante) and (ii) brines with $\delta^{18}O\text{-}H_2O$ / $\delta D\text{-}H_2O$ values, other than seawater. Thus, only the L'Atalante basin appears to exhibit 'seawater dissolution' scenario. The $\delta^{18}O\text{-}H_2O$ values of other Mediterranean deep-sea brine pools are significantly enriched relative to $\delta D\text{-}H_2O$, indicating that this shift cannot be caused by evaporation of modern seawater. It is very likely that they arose from older underground brine masses formed in the past by the contact of various layers of the evaporitic suite with subterranean interstitial water. This genesis is most likely for Discovery, Hephaestus and Kryos basins, since the existence of magnesium-rich interstitial brine pools, occurring in sediments at depths > 300 m, was confirmed more than 20 years ago in the Mediterranean Ridge region (Vengosh et al., 1994) with values of the latter two brines indistinguishable from each other, thus indicating the common source of their nutrition. This conclusion was further confirmed by plotting the average composition of Mediterranean deep-sea brines along the seawater evaporation path (Fig. 10 b-d). As with the isotopic analysis, a plot of main ions versus bromine showed that although the Discovery brine is very similar in chemical composition to the Hephaestus and Kryos brines, it is noteworthy that the chemistry of the latter was again indistinguishable from each other, which indicates that Hephaestus and Kryos originated from a common source.

6.6. Comparative biomolecular analysis of Hephaestus and Kryos interfaces

The brines of Discovery, Hephaestus and Kryos are sterile and considered anathema to life due to the extremely high chaotropicity (entropic disordering of biomolecules) and contrasting thermodynamic availabilities of water (extremely low water activity, a_w) of their $MgCl_2$-saturated brines. Indeed, Mg^{2+} cation is one of the strongest chaotropic agents that cause a disruption to the ordering of water molecules, and act to destabilize proteins, inhibit enzymes, solubilize membranes, and at high concentrations (>2.5 M) can lead to cell death (Fisher et al., 2021; Hallsworth, 2022; La Cono et al., 2019; Yakimov et al., 2015). Although Cl^- binds far more weakly compared with the most chaotropic anions (SCN^- and I^-), nonetheless, the large concentrations of Cl^- in the athalassohaline *Discovery*, *Hephaestus* and *Kryos* brines (upwards of 10 M) completely inhibits enzyme and cellular function (Hallsworth et al., 2007).

In addition to chaotropicity, the microbial life within athalassohaline brines of Discovery, Hephaestus and Kryos is also limited by a very low water activity ($a_w \sim 0.4$) (Edgcomb et al., 2009; Hallsworth et al., 2007; La Cono et al., 2019; Yakimov et al., 2015) due to the high solubility of $MgCl_2$ leading to high ionic strength waters. This also leads to increased osmotic stress and an elevated concentration of high charge-to-size ratio Mg^{2+} ions. Small divalent cations, such as Mg^{2+}, form strong hydration shells in solution leaving less available water for cellular processes (Fisher et al., 2021). Cell division has never been observed at a_w lower than 0.585, a current record held by the fungus *Aspergillus penicillioides* (Grant, 2004; Stevenson et al., 2015; Hallsworth, 2022). Therefore, only the interfaces of Hephaestus and Kryos brine pools provide a refuge for magnesium-adapted prokaryotic communities and only these compartments, separating $MgCl_2$-rich brines from seawater were taken into account when searching for signs of life. Among different types of nucleic acids, the recovery and analyses of both messenger and ribosomal RNA (mRNA and rRNA) molecules were taken into account (Hallsworth et al., 2007; Yakimov et al., 2015; La Cono et al., 2019). This was done because double stranded DNA (dsDNA) has been shown to be a type of biological molecules that is well preserved in highly chaotropic environments

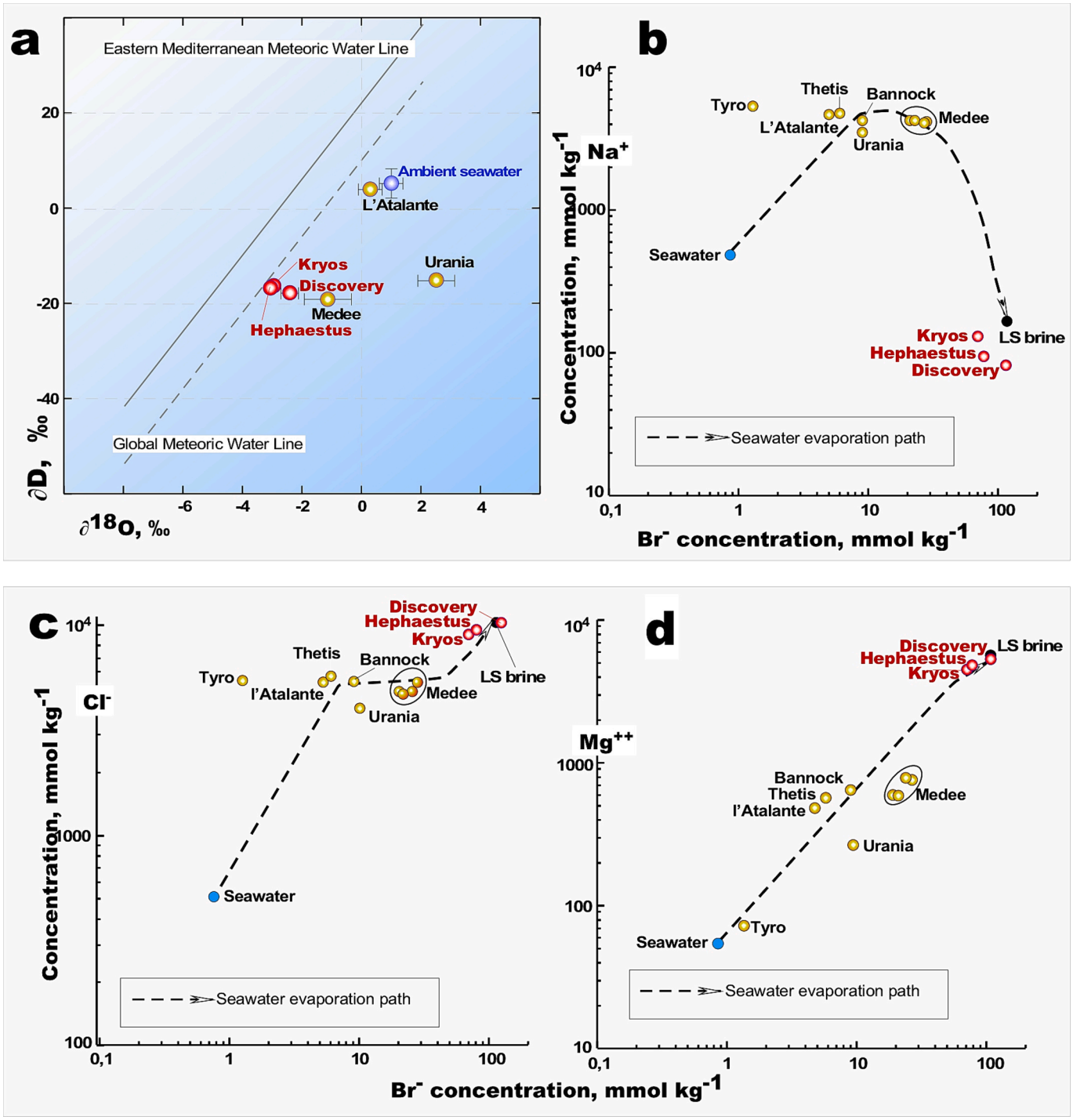

Fig. 10. Plot of δD versus $\delta^{18}O$ for brine samples collected in DHALs Discovery, Hephaestus, Kryos, L'Atalante, Medee and Urania (a). Eastern Mediterranean seawater values, measured in the seawater, overlaying the lakes, are shown as blue bubble. The solid and dashed lines represent Eastern Mediterranean Water Line and Global Meteoric Water Lines, respectively. Evaporation path of seawater in the Na^+ vs. Br^- (b); Cl^- vs. Br^- (c) and Mg^{2+} vs. Br^- plots (d). Average brine compositions have been indicated as yellow bubbles for thalassohaline DHALs and as red bubbles for $MgCl_2$-filled athalassohaline brines Discovery Hephaestus and Kryos. LS brine is the latest stage brine, occurred when seawater is evaporated to less than 1 % of its volume. Data taken from de Lange et al. (1990), La Cono et al. (2019), Yakimov et al. (2015). (For interpretation of the references to color in this figure legend, the reader is referred to the web version of this article.)

(Hallsworth et al., 2007) and although present in the basins, could not necessarily originate from autochthonous actively thriving microbiota, but also from metabolically inactive or dead seawater microbiota, which enters the basins in the form of settling microparticles called 'ocean snow' and distorts the real picture of microbial life actively functioning in the interface ecosystem.

Following the specific aims of the present study, the taxonomic diversity of rRNA-containing microbial population recovered from the low level of Hephaestus interface was compared with that of *Kryos*. Despite the same number of sequences analyzed, alpha diversity analysis revealed a clear pattern of differentiation of microbial communities. Microbiota of Kryos shows significantly higher diversity than Hephaestus in both amplified sequence variants (ASVs) (32 vs. 12) and Inverse Simpson and Shannon indices (Table 4). As a consequence,

Table 4
Alpha diversity indices calculated for *Kryos* and *Hephaestus* interfaces.

Sample ID	Number of Sequences*	Number of ASVs**	Inverse Simpson Diversity Index	Shannon Diversity Index	Chao1 Richness Estimator
Kryos	155	32	6.33	2.21	18.6
Hephaestus	153	12	3.07	1.43	8.0

* Sequences remaining after quality filtering, and removal of chimeric sequences.
** ASVs passed quality filtering.

Chao1 richness estimator, calculated for Kryos was 2.33 higher than that of Hephaestus interface (18.6 vs. 8.0).

In terms of 16S rRNA phylogeny, the prokaryotic community of Hephaestus interface resembled the seawater-brine interfaces of Discovery and Kryos (Hallsworth et al., 2007; La Cono et al., 2019; Yakimov et al., 2015), further hinting at the existence of hitherto uncharacterized hyper-halophiles adapted to resist the Mg^{2+} chaotropicity and capable of metabolic activity under harsh athalassohaline conditions. Similar to the latter, the Hephaestus interface is dominated by acetogenic representatives of the bacterial KB1 group (Nigro et al., 2016), recently assigned to *Acetothermia* (phylum *Bipolaricaulota*) and of the extremely halophilic sulfate reducers of the phylum *Desulfobacterota*. However, this is where the similarities between the two ecosystems end and the Kryos bacterial community is additionally represented by at least six more higher taxonomic groups belonging to the phyla *Bacteriodota*, *Chloroflexota*, *Elusimicrobiota*, *Patescibacteria*, *Pseudomonadota* and *Verrucomicrobiota*, all of them completely absent in the Hephaestus interface (Fig. 11a).

The same trend was found when comparing the archaeal diversity between both ecosystems (Fig. 11b). Both interfaces are dominated by members of the MSBL1 *Candidate Division*, recently assigned to Hadarchaeota, and by the representatives of the genus *Methanohalophilus,* currently belonging to the phylum *Halobacteriota*. Both of these archaeal groups are likely involved in the methane production in the Hephaestus and Kryos ecosystems. Indeed, while the former organisms are thought to perform methanogenesis (Borin et al., 2009), the latter are a well-known and well-studied group of methylotrophic methanogens (Nigro et al., 2016). All *Hadarchaeota*-related sequences found in the Hephaestus interface belong to two distinct clades also present in Kryos. However, the Kryos interface hospitalizes two additional, deeply branched clades of *Hadarchaeota* that absent from Hephaestus (Fig. 11b). The *Methanohalophilus* group was represented at both interfaces by two closely related clades, also present at the Discovery interface and in the Urania basin thalassohaline brine (Fig. 11b), suggesting that only a few methylotrophic methanogens are able to function in extreme salinity anoxic environments, reflecting their low diversity. Similar low diversity was observed in haloarchaeal members of the genus *Halorhabdus* shared by the Hephaestus and Kryos ecosystems. It should be noted that this clade appears to be specific to athalassohaline environments, as distantly related haloarchaea was found only in Discovery and were absent from either thalassohaline basins. Both interfaces appear to be optimal ecological niches for *Candidate Phylum* Nanohaloarchaeota, a recently described and cultivated phylum of extremely halophilic anaerobic ultrasmall (<500 nm in size) archaea (La Cono et al., 2020; La Cono et al., 2023). They were represented by numerous sequences divided into two distinct clades, both of which are common to the Hephaestus and Kryos interfaces (Fig. 11b). These clades are deeply diversified with all know nanohaloarchaea, representing a new, class-level taxonomic clade. Finally, the Kryos archaeal community is additionally represented by members of the *Candidate Phylum* Aenigmarchaeota, a second group of ultra-small archaea that are completely absent from Hephaestus. This further supports our hypothesis that the Hephaestus microbiota has its roots in the microbial community of Kryos, which was only partially transferred to Hephaestus from its northern part, probably during the triggering CE 365 earthquake accompanied by large-amplitude internal waves, as we propose in the present study.

7. Discussion

Sediment within the brine filled Hephaestus basin reveals a stratigraphy including four main modes of deposition. From bottom to top these are: i) laminated pelagic sediment representing 15 % of the core; ii) a slump deposit accounting for 45 % of the total sediment thickness; iii) a turbidite bed occupying 25 % of the core; iv) brine bearing anoxic sediment constituting the topmost 7 % of the core. In our interpretation, both the slump and turbidite were emplaced during the tsunamigenic CE 365 $M > 8$ earthquake, which likely had significant effects in the relatively near (about 100 km) Hephaestus basin and surrounding region.

Earthquakes can trigger sediment remobilization hundreds of kilometers from the epicenter, depending on seismic loading and slope stability. It is recognized that 0.1–0.2 g PGA (peak ground acceleration) is the threshold of stability for mobilization of surface sediments and generation of turbidity currents in the Marmara Sea (Çağatay et al., 2025) while calculation of PGAs for large historical earthquakes indicates that PGA > 0.6 g is necessary for turbidite deposition along the northern Japan trench (Ikehara et al., 2023). Shake maps of Crete-type $M > 8$ earthquakes occurred worldwide since 2000 are generally associated with PGA between 0.1–0.8 g at about 100 km from the epicenter with PGA values up to 0.5–0.8 g for earthquakes with $M > 8$ (SM8). Moreover, during the 2016 Kaikōura M_w7.8 earthquake threshold PGVs (peak ground velocities) for triggering turbidity currents was estimated in the range 16–25 cm/s (Howarth et al., 2021), velocities that are comparable to those reported for Crete-type earthquakes at 100 km distance from the epicenter (SM8). These values thus result high enough to trigger slope instability. Both the slump and turbidite bed in our core might be related to seismic shaking during the Crete earthquake.

Surface disruption and slope instabilities can also be triggered by liquefaction resulting from intense and prolonged earthquake shaking (Obermeier, 2009) depending on distance from the epicenter, soil type, initial confining pressure, and margin slope. Since the farthest liquefaction effects for an earthquake with a magnitude $M_w = 8$ are estimated to extend up to approximately 300 km (Obermeier, 1996) it follows that the CE 365 Crete earthquake likely triggered liquefaction effects in isolated basins of the Mediterranean Ridge further enhancing slope-instability processes. The occurrence of landslides within the brine lakes may have generated large-amplitude waves of the brine-water interface. Gravity-driven sediment flows striking a brine lake with a density difference between the brine and overlying seawater, in fact, can generate large-amplitude internal waves if they are relatively fast (Monaghan et al., 1999; Rimoldi et al., 1996; Sawyer et al., 2019).

The slump and the turbidite in core KR2_2 include black patches of evaporitic material (bischofite, halite, gypsum, SM7) that were probably remobilized during seismic shaking and slope failures. We suggest two different scenarios that might explain why evaporitic material is included in such deposits: i) brine leaching from the sub-seafloor during seismic shaking; ii) brine spillover from another basin that was anoxic before the CE 365 event. Due to the lack of data on the Kryos basin sediment, it is currently not possible to determine its age and how it formed, thereby preventing a definitive assessment of the most likely scenario.

Bischofite is a highly hygroscopic late-stage evaporitic mineral that dissolves upon contact with underground water. As a result, buried deposits of solid bischofite can be easily converted into lenses of magnesium-rich subsurface brines underlying Mediterranean Ridge sediments (Vengosh et al., 1994). Although it is unknown how long the dissolved bischofite remained in this way as interstitial pools, we cannot exclude the possibility that the brines within the Hephaestus slump and turbidite bed were expelled to the seafloor through vents or cracks

Fig. 11. Phylogenetic tree of bacterial (a) and archaeal (b) 16S rRNA gene sequences. Bootstrap values greater than or equal to 70 % appear as solid circles, those less than 70 % and greater than 60 % appear as white circles. Sequences retrieved from the Hephaestus and Kryos seawater: brine interfaces are shown in green and red colors, respectively. (For interpretation of the references to color in this figure legend, the reader is referred to the web version of this article.)

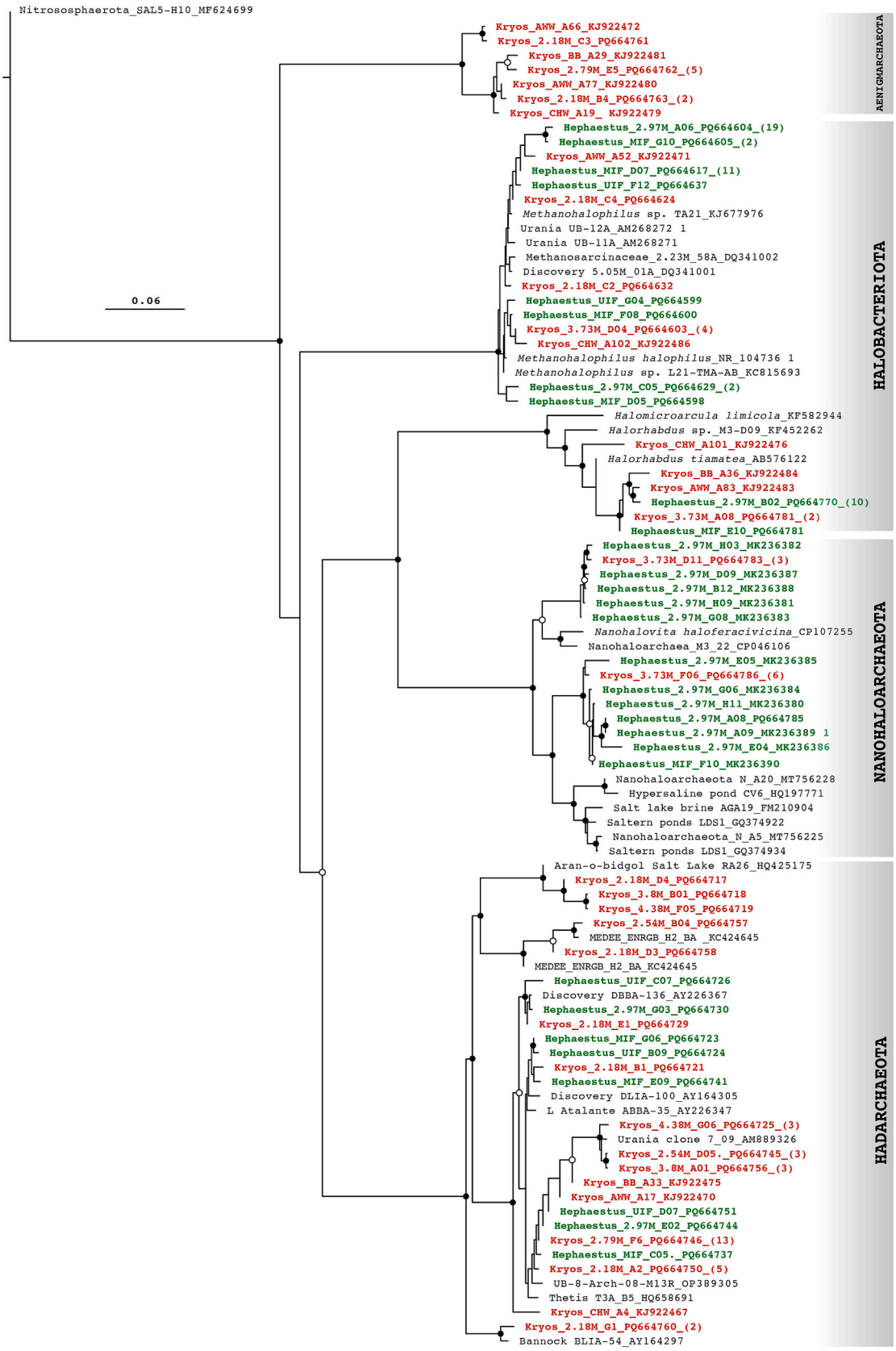

Fig. 11. (*continued*).

during the CE 365 earthquake. However, sediment pore water analyses in the Hephaestus basin, indicated that Mg^{2+} and Cl^{-} concentrations decrease sharply with sediment depth and the deepest area of the Hephaestus basin fits perfectly into a one-dimensional diffusive transport model (La Cono et al., 2019), that implies downward diffusion of brine from the surface into the sediments. In this context, the extremely

viscous and dense bischofite brine of the Hephaestus basin might have formed at an indeterminate time outside the Hephaestus depression and subsequently incorporated in its sedimentary sequence during the high energy event. Large amplitude waves generated at the brine interface of neighboring brine lakes and spreading out evaporitic material in a larger region seems to be the most realistic scenario. The Mg-calcite and bishofite present in Unit C might thus be related to such waves while anoxic sediments in the Hephaestus depression resulted at the end of the catastrophic event. The bathymetric threshold between Kryos and Hephaestus requires waves exceeding 80 m (Fig. 2) well below the amplitude of interface waves described in the Orca Basin brine lakes (Gulf of Mexico), where ~200 m amplitude waves were generated by submarine landslides (Sawyer et al., 2019).

Monaghan et al. (1999) demonstrated, through both laboratory experiments and numerical simulations, that a fast-moving landslide encountering a brine layer with a relatively small density difference from the seawater can efficiently generate large internal waves. When sediment-driven gravity currents impact a stratified two-layer system, they can induce oscillations at the brine interface, with wave amplitude described by:

$$a \approx (\rho_{slide} \times v_{slide}^2) / (\Delta_{\rho f} \times g) \quad (1)$$

In this formulation, ρ_{slide} refers to the density of the landslide material, v_{slide} indicates its velocity, $\Delta_{\rho f}$ represents the density difference between seawater and brine, and g denotes gravitational acceleration. The equation originates from an energy balance perspective, where the advancing flow causes upward displacement of the interface by forcing fluid to rise around the leading edge of the landslide (Monaghan et al., 1999; Monaghan, 2007). For a comprehensive treatment of the underlying dynamics as applied to the Orca Basin case consult Sawyer et al. (2019).

In the case of the Hephaestus Basin, $\Delta_{\rho f}$ is known and equal to 320 kg/m^3 (density of the brine = 1320 kg/m^3, La Cono et al., 2019). Estimates of submarine landslide velocities are commonly based on measurements from past events and associated turbidity current dynamics (Heezen and Ewing, 1952; Ryan and Heezen, 1965; De Blasio et al., 2005; Heinrich et al., 2001). In the case of the Hephaestus Basin, the landslide is inferred to have been relatively fast-moving, based on the notably steep slopes (up to 11-12° SM5). As a result, we adopt a conservative lower-bound velocity estimate of 10 m/s, and an upper-bound estimate of 20 m/s as done for the Orca basin where slopes are 12° steep on average (Sawyer et al., 2019). Since the precise density of the landslide material is unknown, we provide solutions to Eq. 1 across a plausible range of values (Fig. 12), based on sediment core data from ODP Site 969 in the Eastern Mediterranean, near the Hephaestus Basin (Emeis et al., 1996). These data indicate that sediment density increases from around 1400 kg/m^3 at the seafloor to roughly 2000 kg/m^3 at depths of about 100 m below the surface. For this preliminary analysis, local heterogeneities such as sapropels or tephra layers are not considered, as they could introduce variability in specific strata.

Accordingly, using Eq. 1 and assuming a landslide velocity of 10 m/s, with sediment densities ranging from 1400 to 2000 kg/m^3, the resulting wave amplitude at the brine interface is estimated to fall between 45 m and 64 m. If the velocity increases to 20 m/s, the corresponding wave amplitude ranges from 178 m to 254 m (see Fig. 12). Considering that the sill between the Hephaestus and Kryos basin is about 80 m we deduce that v_{slide} > 11,2–13,4 m/s are capable to trigger brine spillover from Kryos to Hephaestus (Fig. 12). The wave amplitudes predicted by this model for the Hephaestus brine lake are on the same order of magnitude as those observed in other oceanographic settings (Alford et al., 2015; Huang et al., 2016; Reeder et al., 2011).

Brine diffusion and the onset of anoxia triggered by the CE 365 Crete earthquake may have impacted other anoxic basins in the Mediterranean Sea, potentially leading to their formation or restructuring during this catastrophic event. For instance, the onset of anoxia in the Discovery Basin, was estimated at around 2000 years ago (Wallmann et al., 1997) while a connection between the Urania basin brines and a major earthquake dated to 1650 y BP was already proposed (Goldhammer

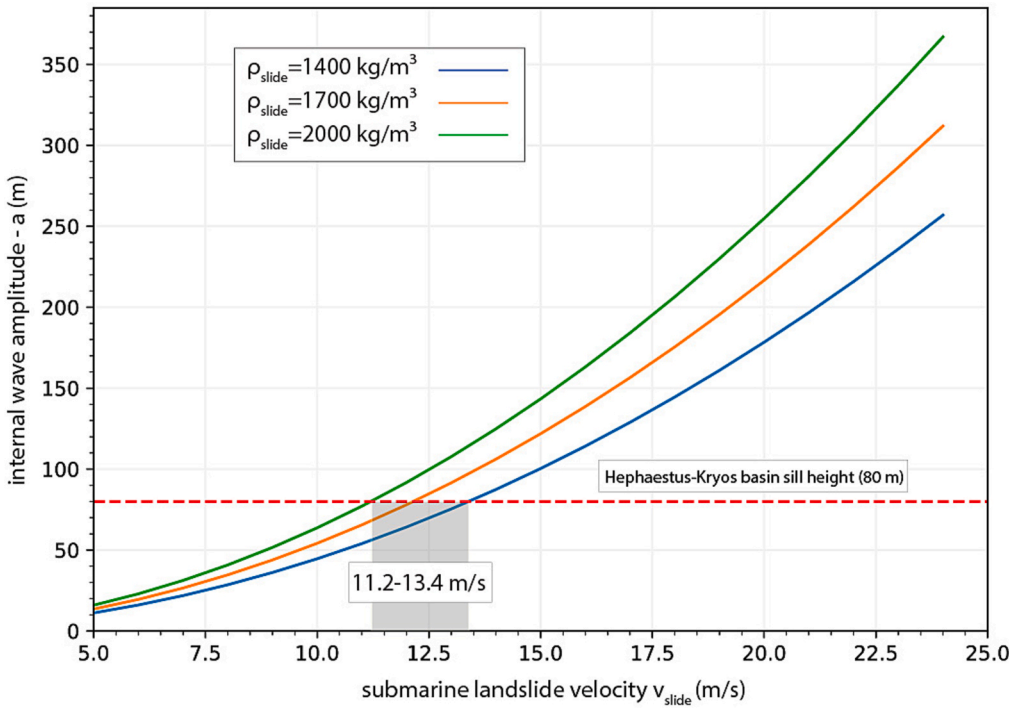

Fig. 12. Predicted maximum wave amplitude produced by impact of submarine landslides in the Kryos brine lake as a function of landslide velocity (Eq. 1; Monaghan et al., 1999). Solutions are shown for three values of landslide density (ρ_{slide}) based on sediment core data from ODP Site 969 in the Eastern Mediterranean, near the Hephaestus Basin (Emeis et al., 1996). The spill point of the Kryos basin (dashed red line) is 80 m above the seawater-brine interface (Fig. 2). (For interpretation of the references to color in this figure legend, the reader is referred to the web version of this article.)

et al., 2015), in close agreement with the timing of the CE 365 Crete event. Similarly, in the Red Sea brine pools, although their origin is hydrothermal, it has been proposed that the emplacement of the brines may have been mediated by seismic activity (Purkis et al., 2022; Schmidt et al., 2015).

The observed concentrations of Mg^{2+} and Cl^- in the Hephaestus basin suggest that its surface sediments were in contact with $MgCl_2$ brines for no more than 700–1000 yr (La Cono et al., 2019), making them younger than the Crete event. However, such a young age may indicate the last perturbation of the brines rather than brine inception. Approximately 700 yr BP (CE 1303), a major earthquake occurred on the eastern side of Crete with a magnitude of $M > 8$. This earthquake, which did not trigger sediment slumping at a basin scale as evidenced by the lack of coeval turbidites in the stratigraphic record (Polonia et al., 2022, 2016), might have produced fluid flow in the subsurface that are detected in the PW profile within the Hephaestus basin giving rise to a rejuvenated geochemical signature.

To summarize, core KR2_2 suggests that during the Crete earthquake resedimented particles were originated from the steep walls of the basin that was not anoxic before such event, while violent expulsions of fluids might have caused the collapse of entire sections of the seafloor within adjoining anoxic basins such as Kryos as evidenced by slumped material and instability processes (SM5). The extremely viscous and dense bischofite brine formed nearby outside at an indeterminate time and only during the Crete earthquake settled in the *Hephaestus* depression. The heterogeneous composition of the organic material further supports the occurrence of large-scale remobilization. Based on the overall organic matter composition, the direct advection of terrestrial-rich sediment can be excluded. Instead, the sediment source is more compatible with deposits characterized by a diverse range of ages and, thus, a complex and diverse composition. The submarine landslides might have triggered large-amplitude waves at the brine interface with brine spillover from the Kryos to the Hephaestus basin (Fig. 13). The CE 365 mega-tsunami associated with the Crete earthquake further enhanced the resedimentation of large volumes of Pleistocene deposits as described in the Urania basin (Aiello et al., 2020), Tyro Basin (Polonia et al., 2016) and many other abyssal basins of the Ionian Sea (Polonia et al., 2022). In addition, while the upper Unit E exhibited an oily-like texture, suggesting potential fluid escape of thermally mature OC during the earthquake, our analyses ruled out the oil influence (SM2) and further confirmed the anoxic environment as a result of the brine-rich and dense bottom waters.

Our hypothesis that Hephaestus basin owes its birth to seismic activity and transfer of brine from nearby Kryos basin was confirmed by isotopic and biomolecular analysis of both these brines. Based on the comparative biomolecular analysis, we can conclude that, despite the youth of the Hephaestus basin, its interface is populated by very diverse enigmatic prokaryotes, adapted to withstand the above-mentioned polyextremophily. Although these obligate anaerobic halophilic communities are quite distinct from seawater microbes, they are strikingly

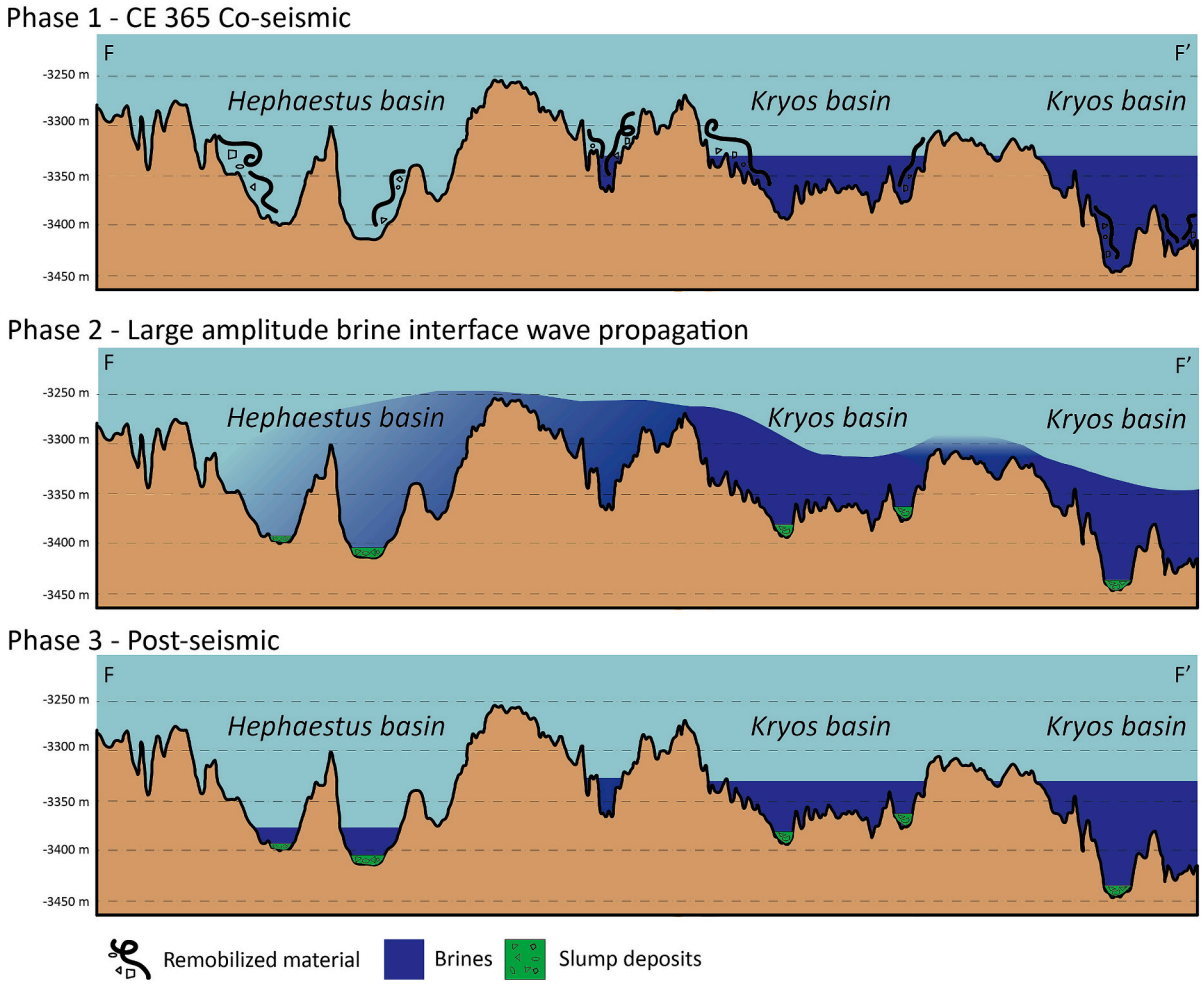

Fig. 13. Bathymetric profile F-F' across the Kryos and Hephaestus basins (see Fig. 2 for its location) and the conceptual model showing: Phase 1) CE 365 Crete earthquake-generated processes; Phase 2) propagation of a large amplitude wave of the brine interface generated by slope failures within the Kryos basin; Phase 3) the resulting brines filling the Kryos and Hephaestus basins. No brine pool developed in the small basin between Kryos and Hephaestus because the depth of this basin is above the brine-interface depth in the Hephaestus lake and thus brines do not preserve.

similar to the microbiota of the Kryos interface. However, the latter basin harbors a more diverse microbial community, which refutes the hypothesis of a common origin of both basins from a unique reservoir of ancient $MgCl_2$-saturated groundwater. To explain the puzzle of only partial similarity of the two microbial communities and the presence of a minimized microbiota in Hephaestus, we propose that the microbiota of Hephaestus originates from the microbial community of Kryos, which was transported to Hephaestus from its northern part and only partially survived the perturbation during the earthquake and tsunami, accompanied by significant mixing of all layers of the highly stratified microbial community of the interface of Kryos with deadly brine saturated with $MgCl_2$.

If the microbial diversity in these two lakes, Kryos and Hephaestus, is strikingly similar, our assumption about the inheritance of the microbial community is only a hypothetical observation, which is not yet supported by any scientifically substantiated concrete data. It should be noted that, given the enormous difficulty of collecting the seawater-brine interface samples from these deep-sea lakes, which are among the most inaccessible places on our planet, it is no coincidence that both these lakes were discovered only recently (La Cono et al., 2019; Yakimov et al., 2015). Thus, an accurate comparison of the two ecosystems based on direct DNA tracking analysis is extremely difficult and extremely challenging. Nevertheless, we plan in the near future to conduct a metagenomic analysis and, additionally, to perform the taxon-specific CRISPR identification and spacers extraction from the metagenome using CRISPRCasFinder. It is known that bacterial and archaeal defense systems, such as CRISPR, are based on the recognition of DNA fragments of attacking viruses encoding conserved structural and morphogenetic viral proteins (Zhou et al., 2025). To establish relationships between lake-derived viruses and bacterial and archaeal groups, CRISPR spacers will be used as queries for BLASTn searching of viral sequences. A viral sequence that exactly matches a certain spacer will be considered as the target sequence of the spacer (i.e., protospacer), and the spacer-associated bacterial or archaeal taxon will be assigned as a host group for the corresponding viral sequence bearing the protospacer. If some members of a group of closely related viruses have been exposed to CRISPR spacers, all members of that group will be considered to infect the same hosts, and therefore those hosts are or were in the past members of the same ecosystem.

8. Conclusions

Sedimentological, micropaleontological, and geochemical analyses conducted on a 3.5 m long gravity core retrieved from the Hephaestus anoxic basin offer insights into the timing, sedimentary processes, and mechanisms driving seafloor anoxia within the brine lake. Our findings highlight the pivotal role of tectonic activity and seismic shaking in basin evolution and brine formation.

The analyzed samples document ~200 kyr of sedimentation encompassing pelagic intervals, sapropelitic sediments, slump deposits, chaotic layers, turbidite beds, and a recently deposited anoxic and viscous topmost sediment unit. Trends in lignin phenols and cutin acids indicate a complex terrestrial input and the influence of multiple reworked sources, underscoring intricate interactions between terrestrial and marine processes that have shaped the sedimentary record of the brine lake.

- Background marine conditions are reflected in the laminated pelagic sediment at the base of the sediment core representing 15 % of the total sediment thickness.
- Topmost seafloor anoxia is represented by black and viscous brine bearing sediment constituting the 7 % of the core.
- The transition from oxic sediments at the core bottom to the recent anoxic conditions is marked by a ~2 m thick (70 % of the total thickness) stacked slump/turbidite deposit with a complex structure.

The multi-sourced resedimented deposit was emplaced during a catastrophic event that mobilized sediment from both abyssal and coastal environments in the time window CE 155-439 as deduced through radiometric dating.

Based on the organic matter composition, a river-dominated source can be excluded, and thus seismic shaking and tsunami propagation are the more likely mechanisms that triggered sediment remobilization. Based on historical descriptions and sedimentary records, the only event capable of triggering resedimented deposits in the reported time window is the CE 365 M > 8 Crete earthquake and related tsunami that produced large-scale sediment remobilization in the entire Eastern Mediterranean Sea.

The presence of evaporitic material within the CE 365 slump and turbidite bed suggest brine leaching from the sub-seafloor during seismic shaking or brine spillover from another basin that was anoxic before the CE 365 event. Since sediment pore water analyses imply downward diffusion of brine from the surface into the sediments, bischofite brines probably formed at an indeterminate time outside the Hephaestus depression and were subsequently incorporated in its sedimentary sequence during the high energy event.

In this reconstruction, large amplitude internal waves generated at the brine interface of the neighboring Kryos lake, and enhanced brine spillover from Kryos to Hephaestus basin. Biomolecular analysis shows that, despite the youth of the Hephaestus basin, its interface is populated by very diverse enigmatic prokaryotes and anaerobic halophilic communities that, most likely, have their roots in the Kryos microbiota, which was only partially transported to Hephaestus. While brine lakes are assumed to be stable environments, external forces such as strong earthquakes along the Hellenic Arc, can cause significant disturbances of the anoxic environment and injection of gravity flows into the sedimentary basin triggering brine spillover to the surrounding depressions.

This study highlights the profound impact of seismic activity on the stability of deep-sea anoxic basins and provides broader insights into geohazards, planetary analogues, and subsurface life. The evidence that a single mega-earthquake, such as the CE 365 M > 8 Crete event, can remobilize large volumes of sediment, trigger brine spillover, and remodel entire basin environments, underscores the vulnerability of deep ecosystems to tectonic perturbations. The dynamic behavior of brine lakes like Hephaestus and Kryos offers valuable analogues for transient hypersaline environments on Mars, where past seismic or impact-induced perturbations may have facilitated brine migration and the formation of potential habitable niches. Finally, the rapid colonization of the Hephaestus brine interface by complex and diverse microbial communities, likely inherited from adjacent systems, sheds light on the resilience and mobility of deep biosphere life. Throughout Mars' evolution, its geological, climatic and paleohydrological conditions have been similar to those of Earth, suggesting that Mars has had or still has environments, such as hypersaline subsurface lenses or subglacial brines, capable of supporting life (Hallsworth et al., 2021). This suggests that subsurface microbial ecosystems on Earth, and perhaps on other planets, can persist in the face of geological upheaval, opening up promising avenues for the search for life beyond our planet.

CRediT authorship contribution statement

A. Polonia: Writing – original draft, Validation, Supervision, Resources, Project administration, Methodology, Investigation, Funding acquisition, Formal analysis, Data curation, Conceptualization. **A. Asioli:** Writing – original draft, Validation, Methodology, Investigation, Formal analysis, Data curation, Conceptualization. **L. Ferraro:** Writing – original draft, Validation, Methodology, Investigation, Formal analysis, Data curation, Conceptualization. **E. Colizza:** Writing – original draft, Validation, Methodology, Formal analysis, Data curation. **F. Corticelli:** Writing – original draft, Validation, Methodology, Formal analysis, Data curation. **G.J. de Lange:** Writing – original draft, Validation, Methodology, Formal analysis, Data curation. **A. Gallerani:** Writing – original

draft, Validation, Methodology, Investigation, Formal analysis, Data curation. **G. Gasparotto:** Writing – original draft, Validation, Methodology, Investigation, Formal analysis, Data curation. **L. Gasperini:** Writing – original draft, Validation, Software, Methodology, Investigation, Formal analysis, Data curation. **G. Giorgetti:** Writing – original draft, Validation, Methodology, Formal analysis, Data curation. **V. La Cono:** Writing – original draft, Validation, Investigation, Funding acquisition, Formal analysis, Data curation, Conceptualization. **G. La Spada:** Writing – original draft, Validation, Methodology, Formal analysis, Data curation. **T. Tesi:** Writing – original draft, Validation, Methodology, Formal analysis, Data curation. **M. Yakimov:** Writing – original draft, Validation, Methodology, Investigation, Funding acquisition, Formal analysis, Data curation, Conceptualization.

Acknowledgments

Chirp data processing and structural mapping was performed using the open software SeisPrho (Gasperini and Stanghellini, 2009), freely available at http://software.bo.ismar.cnr.it/seisprho. XRF data were collected in the ISMAR-CNR geochemical laboratory. We sincerely thank the Editor Prof. Nicholas Rawlinson and two anonymous reviewers for their constructive and insightful comments, which greatly improved the quality and clarity of this manuscript. This work is dedicated to Giovanni Bortoluzzi, on the tenth anniversary of his passing. The acquisition of geophysical data and sediment samples in the Hephaestus Basin was made possible through his remarkable curiosity and invaluable contribution. His expertise, dedication, and vision have left a lasting legacy in advancing scientific research in the Mediterranean Sea. His pioneering work in addressing complex scientific challenges in this region continues to inspire and guide our efforts.

Appendix A. Supplementary material

Supplementary data to this article can be found online at https://doi.org/10.1016/j.gr.2025.10.016.

References

Adams, J., 1990. Paleoseismicity of the cascadia subduction zone: evidence from turbidites off the oregon-washington margin. Tectonics 9, 569–583. https://doi.org/10.1029/TC009i004p00569.

Aharon, P., Roberts, H.H., Snelling, R., 1992. Submarine venting of brines in the deep Gulf of Mexico: observations and geochemistry. Geology 20, 483. https://doi.org/10.1130/0091-7613(1992)020<0483:SVOBIT>2.3.CO;2.

Aiello, I.W., Beaufort, L., Goldhammer, T., Heuer, V.B., Hinrichs, K.-U., Zabel, M., 2020. Anatomy of a 'suspended' seafloor in the dense brine waters of the deep hypersaline Urania Basin. Deep Sea Res. Part II 171, 104626. https://doi.org/10.1016/j.dsr2.2019.07.014.

Alford, M.H., Peacock, T., MacKinnon, J.A., Nash, J.D., Buijsman, M.C., Centurioni, L.R., Chao, S.-Y., Chang, M.-H., Farmer, D.M., Fringer, O.B., Fu, K.-H., Gallacher, P.C., Graber, H.C., Helfrich, K.R., Jachec, S.M., Jackson, C.R., Klymak, J.M., Ko, D.S., Jan, S., Johnston, T.M.S., Legg, S., Lee, I.-H., Lien, R.-C., Mercier, M.J., Moum, J.N., Musgrave, R., Park, J.-H., Pickering, A.I., Pinkel, R., Rainville, L., Ramp, S.R., Rudnick, D.L., Sarkar, S., Scotti, A., Simmons, H.L., St Laurent, L.C., Venayagamoorthy, S.K., Wang, Y.-H., Wang, J., Yang, Y.J., Paluszkiewicz, T., (David) Tang, T.Y., 2015. The formation and fate of internal waves in the South China Sea. Nature 521, 65–69. https://doi.org/10.1038/nature14399.

Papazachos, B.S., 1996. Large seismic faults in the Hellenic arc. Ann. Geophys. 39. https://doi.org/10.4401/ag-4023.

Bahrouni, N., Meghraoui, M., Bayraktar, H.B., Lorito, S., Zagrarni, M.F., Polonia, A., Bel Mabrouk, N., Kamoun, F., 2024. Tsunami deposits in Tunisia contemporaneous of the large 365 CE Crete earthquake and Mediterranean Sea catastrophic event. Sci. Rep. 14, 4537. https://doi.org/10.1038/s41598-024-53225-7.

Behrmann, J.H., 1991. Conditions for hydrofracture and the fluid permeability of accretionary wedges. Earth Planet. Sci. Lett. 107, 550–558. https://doi.org/10.1016/0012-821X(91)90100-V.

Borin, S., Brusetti, L., Mapelli, F., D'Auria, G., Brusa, T., Marzorati, M., Rizzi, A., Yakimov, M., Marty, D., de Lange, G.J., Van der Wielen, P., Bolhuis, H., McGenity, T. J., Polymenakou, P.N., Malinverno, E., Giuliano, L., Corselli, C., Daffonchio, D., 2009. Sulfur cycling and methanogenesis primarily drive microbial colonization of the highly sulfidic Urania deep hypersaline basin. Proc. Natl. Acad. Sci. 106, 9151–9156. https://doi.org/10.1073/pnas.0811984106.

Bronk Ramsey, C., 2021. OxCal v.4.4.4 [software] [WWW Document].

Bronk Ramsey, C., 2008. Radiocarbon dating: Revolutions in understanding. Archaeometry 50, 249–275. https://doi.org/10.1111/j.1475-4754.2008.00394.x.

Çağatay, M.N., Biltekin, D., Yakupoğlu, N., Güngör, E., Güngör, N., Uçarkuş, G., Henry, P., Polonia, A., Gasperini, L., Grall, C., Acar, D., Ülgen, U.B., Tsabaris, C., Sabuncu, A., 2025. Long–term sedimentary earthquake records along the northern branch of the North Anatolian Fault in the Sea of Marmara (NW Türkiye). Mar. Geol. 489, 107630. https://doi.org/10.1016/j.margeo.2025.107630.

Callahan, B.J., McMurdie, P.J., Rosen, M.J., Han, A.W., Johnson, A.J.A., Holmes, S.P., 2016. DADA2: High-resolution sample inference from Illumina amplicon data. Nat. Methods 13, 581–583. https://doi.org/10.1038/nmeth.3869.

Camerlenghi, A., Cita, M.B., 1987. Setting and tectonic evolution of some Eastern Mediterranean deep-sea basins. Mar. Geol. 75, 31–55. https://doi.org/10.1016/0025-3227(87)90095-8.

Caporaso, J.G., Lauber, C.L., Walters, W.A., Berg-Lyons, D., Huntley, J., Fierer, N., Owens, S.M., Betley, J., Fraser, L., Bauer, M., Gormley, N., Gilbert, J.A., Smith, G., Knight, R., 2012. Ultra-high-throughput microbial community analysis on the Illumina HiSeq and MiSeq platforms. ISME J. 6, 1621–1624. https://doi.org/10.1038/ismej.2012.8.

Capotondi, L., Girone, A., Lirer, F., Bergami, C., Verducci, M., Vallefuoco, M., Afferri, A., Ferraro, L., Pelosi, N., de Lange, G.J., 2016. Central Mediterranean Mid-Pleistocene paleoclimatic variability and its association with global climate. Palaeogeogr. Palaeoclimatol. Palaeoecol. 442, 72–83. https://doi.org/10.1016/j.palaeo.2015.11.009.

Casalbore, D., Chiocci, F.L., Scarascia Mugnozza, G., Tommasi, P., Sposato, A., 2011. Flash-flood hyperpycnal flows generating shallow-water landslides at Fiumara mouths in Western Messina Strait (Italy). Mar. Geophys. Res. 32, 257–271. https://doi.org/10.1007/s11001-011-9128-y.

Chamot-Rooke, N., Rabaute, A., Kreemer, C., 2005. Western Mediterranean Ridge mud belt correlates with active shear strain at the prism-backstop geological contact. Geology 33, 861. https://doi.org/10.1130/G21469.1.

Cita, M.B., 2006. Exhumation of Messinian evaporites in the deep-sea and creation of deep anoxic brine-filled collapsed basins. Sed. Geol. 188–189, 357–378. https://doi.org/10.1016/j.sedgeo.2006.03.013.

Cita, M.B., Kastens, K.A., McCoy, F.W., Aghib, F., Cambi, A., Camerlenghi, A., Corselli, C., Erba, E., Giambastiani, M., Herbert, T., Leoni, C., Malinverno, P., Nosetto, A., Parisi, E., 1985. Gypsum precipitation from cold brines in an anoxic basin in the eastern Mediterranean. Nature 314, 152–154. https://doi.org/10.1038/314152a0.

Cita, M.B., Racchetti, S., Brambilla, R., Bertarini, L., Colombaroli, D., Morelli, L., Negri, M., Ritter, M., Rovira, E., Sala, P., Sanvito, S., 1998. Evoluzione dei bacini profondi del Mediterraneo documentata dalle variazioni nelle velocita di sedimentazione nel Plio-Pleistocene. Rend. Fis. Acc. Lincei 9, 77–94.

Cita, M.B., Vergnaud-Grazzini, C., Robert, C., Chamley, H., Ciaranfi, N., d'Onofrio, S., 1977. Paleoclimatic Record of a Long Deep Sea Core from the Eastern Mediterranean. Quat. Res. 8, 205–235. https://doi.org/10.1016/0033-5894(77)90046-1.

Cordone, A., D'Errico, G., Magliulo, M., Bolinesi, F., Selci, M., Basili, M., de Marco, R., Saggiomo, M., Rivaro, P., Giovannelli, D., Mangoni, O., 2022. Bacterioplankton Diversity and distribution in Relation to Phytoplankton Community Structure in the Ross Sea Surface Waters. Front. Microbiol. 13. https://doi.org/10.3389/fmicb.2022.722900.

Crisafi, F., Smedile, F., Yakimov, M.M., Aulenta, F., Fazi, S., La Cono, V., Martinelli, A., Di Lisio, V., Denaro, R., 2022. Bacterial biofilms on medical masks disposed in the marine environment: a hotspot of biological and functional diversity. Sci. Total Environ. 837, 155731. https://doi.org/10.1016/j.scitotenv.2022.155731.

Dählmann, A., de Lange, G.J., 2003. Fluid–sediment interactions at Eastern Mediterranean mud volcanoes: a stable isotope study from ODP Leg 160. Earth Planet Sci. Lett. 212, 377–391. https://doi.org/10.1016/S0012-821X(03)00227-9.

De Blasio, F.V., Elverhøi, A., Issler, D., Harbitz, C.B., Bryn, P., Lien, R., 2005. On the dynamics of subaqueous clay rich gravity mass flows—the giant Storegga slide, Norway. Mar. Pet. Geol. 22, 179–186. https://doi.org/10.1016/j.marpetgeo.2004.10.014.

de Lange, G.J., Middelburg, J.J., Van der Weijden, C.H., Catalano, G., Luther, G.W., Hydes, D.J., Woittiez, J.R.W., Klinkhammer, G.P., 1990. Composition of anoxic hypersaline brines in the Tyro and Bannock Basins, eastern Mediterranean. Mar. Chem. 31, 63–88. https://doi.org/10.1016/0304-4203(90)90031-7.

de Lange, G.J., ten Haven, H.L., 1983. Recent sapropel formation in the eastern Mediterranean. Nature 305, 797–798. https://doi.org/10.1038/305797a0.

De Rijk, S., Troelstra, S.R., Rohling, E.J., 1999. Benthic foraminiferal distribution in the Mediterranean Sea. J. Foraminiferal Res. 29, 93–103. https://doi.org/10.2113/gsjfr.29.2.93.

Dupré, S., Mascle, J., Foucher, J.-P., Harmegnies, F., Woodside, J., Pierre, C., 2014. Warm brine lakes in craters of active mud volcanoes, Menes caldera off NW Egypt: evidence for deep-rooted thermogenic processes. Geo-Mar. Lett. 34, 153–168. https://doi.org/10.1007/s00367-014-0367-1.

Edgcomb, V., Orsi, W., Leslin, C., Epstein, S.S., Bunge, J., Jeon, S., Yakimov, M.M., Behnke, A., Stoeck, T., 2009. Protistan community patterns within the brine and halocline of deep hypersaline anoxic basins in the eastern Mediterranean Sea. Extremophiles 13, 151–167. https://doi.org/10.1007/s00792-008-0206-2.

Emeis, K.C., Robertson, A.H.F., Richter, C., et al., 1996. Site 969. Proceedings of the Ocean Drilling Program, Initial Reports 160.

Erba, E., Parisi, E., Cita, M.B., 1987a. Stratigraphy and sedimentation in the western Strabo Trench, Eastern Mediterranean. Mar. Geol. 75, 57–75. https://doi.org/10.1016/0025-3227(87)90096-X.

Erba, E., Rodondi, G., Parisi, E., Ten Haven, H.L., Nip, M., De Leeuw, J.W., 1987b. Gelatinous pellicles in deep anoxic hypersaline basins from the Eastern

Mediterranean. Mar. Geol. 75, 165–183. https://doi.org/10.1016/0025-3227(87)90102-2.
Fairbanks, R.G., Wiebe, P.H., 1980. Foraminifera and chlorophyll maximum: vertical distribution, seasonal succession, and paleoceanographic significance. Science 1979 (209), 1524–1526. https://doi.org/10.1126/science.209.4464.1524.
Ferrer, M., Golyshina, O.V., Chernikova, T.N., Khachane, A.N., Martins dos Santos, V.A. P., Yakimov, M.M., Timmis, K.N., Golyshin, P.N., 2005. microbial enzymes mined from the urania deep-sea hypersaline anoxic basin. Chem. Biol. 12, 895–904. https://doi.org/10.1016/j.chembiol.2005.05.020.
Fisher, L.A., Pontefract, A., M. Som, S., Carr, C.E., Klempay, B., E. Schmidt, B., S. Bowman, J., Bartlett, D.H., 2021. Current state of athalassohaline deep-sea hypersaline anoxic basin research—recommendations for future work and relevance to astrobiology. Environ Microbiol 23, 3360–3369. doi: 10.1111/1462-2920.15414.
Friedman, G.M., Sanders, F.E., 1978. Principles of Sedimentology. Wiley, New York.
Gasperini, L., Stanghellini, G., 2009. SeisPrho: an interactive computer program for processing and interpretation of high-resolution seismic reflection profiles. Comput. Geosci. 35, 1497–1507. https://doi.org/10.1016/j.cageo.2008.04.014.
Goldfinger, C., 2011. Submarine paleoseismology based on turbidite records. Ann. Rev. Mar. Sci. 3, 35–66. https://doi.org/10.1146/annurev-marine-120709-142852.
Goldfinger, C., Nelson, C.H., Morey, A.E., Johnson, J.E., Patton, J.R., Karabanov, E.B., Gutierrez-Pastor, J., Eriksson, A.T., Gracia, E., Dunhill, G., Enkin, R.J., Dallimore, A., Vallier, T., 2012. Turbidite event history—Methods and implications for Holocene paleoseismicity of the Cascadia subduction zone. doi: 10.3133/pp1661F.
Goldhammer, T., Schwärzle, A., Aiello, I.W., Zabel, M., 2015. Temporal stability and origin of chemoclines in the deep hypersaline anoxic Urania basin. Geophys. Res. Lett. 42, 4888–4895. https://doi.org/10.1002/2015GL063758.
Goñi, M.A., Montgomery, S., 2000. Alkaline CuO oxidation with a microwave digestion system: lignin analyses of geochemical samples. Anal. Chem. 72, 3116–3121. https://doi.org/10.1021/ac991316w.
Goodman Tchernov, B., Katz, T., Shaked, Y., Qupty, N., Kanari, M., Niemi, T., Agnon, A., 2016. Offshore evidence for an Undocumented Tsunami Event in the 'Low Risk' Gulf of Aqaba-Eilat. Northern Red Sea. Plos One 11, e0145802. https://doi.org/10.1371/journal.pone.0145802.
Grant, K.M., Grimm, R., Mikolajewicz, U., Marino, G., Ziegler, M., Rohling, E.J., 2016. The timing of Mediterranean sapropel deposition relative to insolation, sea-level and African monsoon changes. Quat. Sci. Rev. 140, 125–141. https://doi.org/10.1016/j.quascirev.2016.03.026.
Grant, W.D., 2004. Life at low water activity. Philos Trans R Soc Lond B Biol Sci 359, 1249–66; discussion 1266-7. doi: 10.1098/rstb.2004.1502.
Guidoboni, E., Comastri, A., 1997. The large earthquake of 8 August 1303 in Crete: seismic scenario and tsunami in the Mediterranean area. J. Seismol. 1, 55–72. https://doi.org/10.1023/A:1009737632542.
Hallsworth, J.E., 2022. Water is a preservative of microbes. J. Microbial. Biotechnol. 15, 191–214. https://doi.org/10.1111/1751-7915.13980.
Hallsworth, J.E., Mancinelli, R.L., Conley, C.A., Dallas, T.D., Rinaldi, T., Davila, A.F., Benison, K.C., Rapoport, A., Cavalazzi, B., Selbmann, L., Changela, H., Westall, F., Yakimov, M.M., Amils, R., Madigan, M.T., 2021. Astrobiology of life on Earth. Environ. Microbiol. 23, 3335–3344. https://doi.org/10.1111/1462-2920.15499.
Hallsworth, J.E., Yakimov, M.M., Golyshin, P.N., Gillion, J.L.M., D'Auria, G., De Lima Alves, F., La Cono, V., Genovese, M., McKew, B.A., Hayes, S.L., Harris, G., Giuliano, L., Timmis, K.N., McGenity, T.J., 2007. Limits of life in MgCl2-containing environments: chaotropicity defines the window. Environ. Microbiol. 9, 801–813. https://doi.org/10.1111/j.1462-2920.2006.01212.x.
Heezen, B.C., Ewing, W.M., 1952. Turbidity currents and submarine slumps, and the 1929 Grand Banks [Newfoundland] earthquake. Am. J. Sci. 250, 849–873. https://doi.org/10.2475/ajs.250.12.849.
Heinrich, P.H., Piatanesi, A., Hébert, H., 2001. Numerical modelling of tsunami generation and propagation from submarine slumps: the 1998 Papua New Guinea event. Geophys. J. Int. 145, 97–111. https://doi.org/10.1111/j.1365-246X.2001.00336.x.
Herlemann, D.P.R., Labrenz, M., Jürgens, K., Bertilsson, S., Waniek, J.J., Andersson, A.F., 2011. Transitions in bacterial communities along the 2000 km salinity gradient of the Baltic Sea. ISME J. 5, 1571–1579. https://doi.org/10.1038/ismej.2011.41.
Herut, B., Rubin-Blum, M., Sisma-Ventura, G., Jacobson, Y., Bialik, O.M., Ozer, T., Lawal, M.A., Giladi, A., Kanari, M., Antler, G., Makovsky, Y., 2022. Discovery and chemical composition of the eastmost deep-sea anoxic brine pools in the Eastern Mediterranean Sea. Front. Mar. Sci. 9. https://doi.org/10.3389/fmars.2022.1040681.
Howarth, J.D., Orpin, A.R., Kaneko, Y., Strachan, L.J., Nodder, S.D., Mountjoy, J.J., Barnes, P.M., Bostock, H.C., Holden, C., Jones, K., Cağatay, M.N., 2021. Calibrating the marine turbidite palaeoseismometer using the 2016 Kaikōura earthquake. Nat. Geosci. 14, 161–167. https://doi.org/10.1038/s41561-021-00692-6.
Huang, X., Chen, Z., Zhao, W., Zhang, Z., Zhou, C., Yang, Q., Tian, J., 2016. An extreme internal solitary wave event observed in the northern South China Sea. Sci. Rep. 6, 30041. https://doi.org/10.1038/srep30041.
Ikehara, K., Usami, K., Kanamatsu, T., 2023. Correction: how large peak ground acceleration by large earthquakes could generate turbidity currents along the slope of northern Japan Trench. Prog Earth Planet Sci 10, 15. https://doi.org/10.1186/s40645-023-00549-z.
Jongsma, D., 1987. The geometry and rates of microplate motions in the Eastern Mediterranean Sea — Quantitative constraints by using anoxic basins as piercing points. Mar. Geol. 75, 1–29. https://doi.org/10.1016/0025-3227(87)90094-6.
Jongsma, D., Fortuin, A.R., Huson, W., Troelstra, S.R., Klaver, G.T., Peters, J.M., van Harten, D., de Lange, G.J., ten Haven, L., 1983. Discovery of an anoxic basin within the Strabo Trench, eastern Mediterranean. Nature 305, 795–797. https://doi.org/10.1038/305795a0.
Jorissen, F.J., 1999. Benthic foraminiferal successions across Late Quaternary Mediterranean sapropels. Mar. Geol. 153, 91–101. https://doi.org/10.1016/S0025-3227(98)00088-7.
Kastens, K.A., Cita, M.B., 1981. Tsunami-induced sediment transport in the abyssal Mediterranean Sea. Geol. Soc. Am. Bull. 92, 845. https://doi.org/10.1130/0016-7606(1981)92<845:TSTITA>2.0.CO;2.
Kreemer, C., Chamot-Rooke, N., 2004. Contemporary kinematics of the southern Aegean and the Mediterranean Ridge. Geophys. J. Int. 157, 1377–1392. https://doi.org/10.1111/j.1365-246X.2004.02270.x.
La Cono, V., Bortoluzzi, G., Messina, E., La Spada, G., Smedile, F., Giuliano, L., Borghini, M., Stumpp, C., Schmitt-Kopplin, P., Harir, M., O'Neill, W.K., Hallsworth, J.E., Yakimov, M., 2019. The discovery of Lake Hephaestus, the youngest athalassohaline deep-sea formation on Earth. Sci. Rep. 9, 1679. https://doi.org/10.1038/s41598-018-38444-z.
La Cono, V., Messina, E., Rohde, M., Arcadi, E., Ciordia, S., Crisafi, F., Denaro, R., Ferrer, M., Giuliano, L., Golyshin, P.N., Golyshina, O.V., Hallsworth, J.E., La Spada, G., Mena, M.C., Merkel, A.Y., Shevchenko, M.A., Smedile, F., Sorokin, D.Y., Toshchakov, S.V., Yakimov, M.M., 2020. Symbiosis between nanohaloarchaeon and haloarchaeon is based on utilization of different polysaccharides. Proc. Natl. Acad. Sci. 117, 20223–20234. https://doi.org/10.1073/pnas.2007232117.
La Cono, V., Smedile, F., Bortoluzzi, G., Arcadi, E., Maimone, G., Messina, E., Borghini, M., Oliveri, E., Mazzola, S., L'Haridon, S., Toffin, L., Genovese, L., Ferrer, M., Giuliano, L., Golyshin, P.N., Yakimov, M.M., 2011. Unveiling microbial life in new deep-sea hypersaline Lake Thetis. Part I: Prokaryotes and environmental settings. Environ. Microbiol. 13, 2250–2268. https://doi.org/10.1111/j.1462-2920.2011.02478.x.
La Cono, V., Messina, E., Reva, O., Smedile, F., La Spada, G., Crisafi, F., Marturano, L., Miguez, N., Ferrer, M., Selivanova, E.A., Golyshina, O.V., Golyshin, P.N., Rohde, M., Krupovic, M., Merkel, A.Y., Sorokin, D.Y., Hallsworth, J.E., Yakimov, M.M., 2023. Nanohaloarchaea as beneficiaries of xylan degradation by haloarchaea. J. Microbial. Biotechnol. 16, 1803–1822. https://doi.org/10.1111/1751-7915.14272.
Lourens, L.J., 2004. Revised tuning of Ocean Drilling Program Site 964 and KC01B (Mediterranean) and implications for the δ18O, tephra, calcareous nannofossil, and geomagnetic reversal chronologies of the past 1.1 Myr. Paleoceanography 19. https://doi.org/10.1029/2003PA000997.
Mancinelli, R.L., Fahlen, T.F., Landheim, R., Klovstad, M.R., 2004. Brines and evaporites: analogs for Martian life. Adv. Space Res. 33, 1244–1246. https://doi.org/10.1016/j.asr.2003.08.034.
McClusky, S., Balassanian, S., Barka, A., Demir, C., Ergintav, S., Georgiev, I., Gurkan, O., Hamburger, M., Hurst, K., Kahle, H., Kastens, K., Kekelidze, G., King, R., Kotzev, V., Lenk, O., Mahmoud, S., Mishin, A., Nadariya, M., Ouzounis, A., Paradissis, D., Peter, Y., Prilepin, M., Reilinger, R., Sanli, I., Seeger, H., Tealeb, A., Toksöz, M.N., Veis, G., 2000. Global Positioning System constraints on plate kinematics and dynamics in the eastern Mediterranean and Caucasus. J. Geophys. Res. Solid Earth 105, 5695–5719. https://doi.org/10.1029/1999JB900351.
McMurdie, P.J., Holmes, S., 2013. phyloseq: an R Package for reproducible interactive analysis and graphics of microbiome census data. PLoS One 8, e61217. https://doi.org/10.1371/journal.pone.0061217.
MEDRIFF Consortium, 1995. Three brine lakes discovered in the seafloor of the eastern Mediterranean. Eos, Transactions American Geophysical Union 76, 313–318. doi: 10.1029/95EO00189.
Miramontes, E., Sultan, N., Garziglia, S., Jouet, G., Pelleter, E., Cattaneo, A., 2018. Altered volcanic deposits as basal failure surfaces of submarine landslides. Geology 46, 663–666. https://doi.org/10.1130/G40268.1.
Monaghan, J.J., 2007. Gravity current interaction with interfaces. Annu. Rev. Fluid Mech. 39, 245–261. https://doi.org/10.1146/annurev.fluid.39.050905.110218.
Monaghan, J.J., Cas, R.A.F., Kos, A.M., Hallworth, M., 1999. Gravity currents descending a ramp in a stratified tank. J. Fluid Mech. 379, 39–69. https://doi.org/10.1017/S0022112098003280.
Mouslopoulou, V., Begg, J.G., Polonia, A., Nicol, A., Reston, T.J., Cesca, S., Giba, M., Gasperini, L., 2025. Hellenic subduction system and upper-plate structures revealed by deep high-resolution seismic-reflection profiles and seafloor bathymetry. Tectonics 44. https://doi.org/10.1029/2025TC008943.
Mouslopoulou, V., Begg, J., Nicol, A., Oncken, O., Prior, C., 2015a. Formation of late quaternary paleoshorelines in Crete, eastern mediterranean. Earth Planet. Sci. Lett. 431, 294–307. https://doi.org/10.1016/j.epsl.2015.09.007.
Mouslopoulou, V., Nicol, A., Begg, J., Oncken, O., Moreno, M., 2015b. Clusters of megaearthquakes on upper plate faults control the Eastern Mediterranean hazard. Geophys. Res. Lett. 42. https://doi.org/10.1002/2015GL066371.
Mulder, T., Alexander, J., 2001. The physical character of subaqueous sedimentary density flows and their deposits. Sedimentology 48, 269–299. https://doi.org/10.1046/j.1365-3091.2001.00360.x.
Mulder, T., Syvitski, J.P.M., Migeon, S., Faugères, J.-C., Savoye, B., 2003. Marine hyperpycnal flows: initiation, behavior and related deposits. A review. Mar. Pet. Geol. 20, 861–882. https://doi.org/10.1016/j.marpetgeo.2003.01.003.
Mullineaux, L.S., Lohmann, G.P., 1981. Late Quaternary stagnations and recirculation of the eastern Mediterranean: changes in the deep water recorded by fossil benthic foraminifera. J. Foramin. Res. 11, 21–44.
Narcisco, Á., Flores, J.-A., Cachão, M., Piva, A., Asioli, A., Andersen, N., Schneider, R., 2012. Late Glacial–Holocene transition in the Southern Adriatic Sea: Coccolithophore and Foraminiferal evidence. Micropaleontology 58, 523–538.
Negri, A., Capotondi, L., Keller, J., 1999. Calcareous nannofossils, planktonic foraminifera and oxygen isotopes in the late Quaternary sapropels of the Ionian Sea. Mar. Geol. 157, 89–103. https://doi.org/10.1016/S0025-3227(98)00135-2.
Nigro, L.M., Hyde, A.S., MacGregor, B.J., Teske, A., 2016. Phylogeography, Salinity Adaptations and Metabolic potential of the Candidate Division KB1 Bacteria based

on a Partial Single Cell Genome. Front. Microbiol. 7. https://doi.org/10.3389/fmicb.2016.01266.
Obermeier, S.F., 2009. Chapter 7 Using Liquefaction-Induced and Other Soft-Sediment Features for Paleoseismic Analysis. pp. 497–564. doi: 10.1016/S0074-6142(09)95007-0.
Obermeier, S.F., 1996. Use of liquefaction-induced features for paleoseismic analysis — an overview of how seismic liquefaction features can be distinguished from other features and how their regional distribution and properties of source sediment can be used to infer the location and strength of Holocene paleo-earthquakes. Eng. Geol. 44, 1–76. https://doi.org/10.1016/S0013-7952(96)00040-3.
Orlowski, N., Breuer, L., Angeli, N., Boeckx, P., Brumbt, C., Cook, C.S., Dubbert, M., Dyckmans, J., Gallagher, B., Gralher, B., Herbstritt, B., Hervé-Fernández, P., Hissler, C., Koeniger, P., Legout, A., Macdonald, C.J., Oyarzún, C., Redelstein, R., Seidler, C., Siegwolf, R., Stumpp, C., Thomsen, S., Weiler, M., Werner, C., McDonnell, J.J., 2018. Inter-laboratory comparison of cryogenic water extraction systems for stable isotope analysis of soil water. Hydrol. Earth Syst. Sci. 22, 3619–3637. https://doi.org/10.5194/hess-22-3619-2018.
Panieri, G., Polonia, A., Lucchi, R.G., Zironi, S., Capotondi, L., Negri, A., Torelli, L., 2013. Mud volcanoes along the inner deformation front of the Calabrian Arc accretionary wedge (Ionian Sea). Mar. Geol. 336, 84–98. https://doi.org/10.1016/j.margeo.2012.11.003.
Papadopoulos, G.A., 2011. A Seismic History of Crete: Earthquakes and Tsunamis, 2000 BC – 2011 - The Hellenic Arc and Trench, 1st ed. Ocelotos, Athens.
Papadopoulos, G.A., Daskalaki, E., Fokaefs, A., Giraleas, N., 2007. Tsunami hazards in the Eastern Mediterranean: strong earthquakes and tsunamis in the East Hellenic Arc and Trench system. Nat. Hazards Earth Syst. Sci. 7, 57–64. https://doi.org/10.5194/nhess-7-57-2007.
Pirazzoli, P.A., Laborel, J., Stiros, S.C., 1996. Earthquake clustering in the eastern Mediterranean during historical times. J. Geophys. Res. Solid Earth 101, 6083–6097. https://doi.org/10.1029/95JB00914.
Pirazzoli, P.A., Thommeret, J., Thommeret, Y., Laborel, J., Montag-Gioni, L.F., 1982. Crustal block movements from Holocene shorelines: Crete and Antikythira (Greece). Tectonophysics 86, 27–43. https://doi.org/10.1016/0040-1951(82)90060-9.
Polonia, A., Bonetti, C., Bonetti, J., Çağatay, M.N., Gallerani, A., Gasperini, L., Nelson, C. H., Romano, S., 2021. Deciphering Co-Seismic Sedimentary Processes in the Mediterranean Sea using Elemental, Organic Carbon, and Isotopic Data. Geochem. Geophys. Geosyst. 22. https://doi.org/10.1029/2020GC009446.
Polonia, A., Camerlenghi, A., Davey, F., Storti, F., 2002. Accretion, structural style and syn-contractional sedimentation in the Eastern Mediterranean Sea. Mar. Geol. 186, 127–144. https://doi.org/10.1016/S0025-3227(02)00176-7.
Polonia, A., Melis, R., Galli, P., Colizza, E., Insinga, D.D., Gasperini, L., 2023. Large earthquakes along slow converging plate margins: Calabrian Arc paleoseismicity based on the submarine turbidite record. Geosci. Front. 14, 101612. https://doi.org/10.1016/j.gsf.2023.101612.
Polonia, A., Nelson, C.H., Romano, S., Vaiani, S.C., Colizza, E., Gasparotto, G., Gasperini, L., 2017. A depositional model for seismo-turbidites in confined basins based on Ionian Sea deposits. Mar. Geol. 384, 177–198. https://doi.org/10.1016/j.margeo.2016.05.010.
Polonia, A., Nelson, C.H., Vaiani, S.C., Colizza, E., Gasparotto, G., Giorgetti, G., Bonetti, C., Gasperini, L., 2022. Recognizing megatsunamis in Mediterranean deep sea sediments based on the massive deposits of the 365 CE Crete event. Sci. Rep. 12, 5253. https://doi.org/10.1038/s41598-022-09058-3.
Polonia, A., Panieri, G., Gasperini, L., Gasparotto, G., Bellucci, L.G., Torelli, L., 2013. Turbidite paleoseismology in the Calabrian Arc Subduction complex (Ionian Sea). Geochem. Geophys. Geosyst. 14, 112–140. https://doi.org/10.1029/2012GC004402.
Polonia, A., Vaiani, S.C., de Lange, G.J., 2016. Did the A.D. 365 Crete earthquake/tsunami trigger synchronous giant turbidity currents in the Mediterranean Sea? Geology 44, 191–194. https://doi.org/10.1130/G37486.1.
Purkis, S.J., Shernisky, H., Swart, P.K., Sharifi, A., Oehlert, A., Marchese, F., Benzoni, F., Chimienti, G., Duchâtellier, G., Klaus, J., Eberli, G.P., Peterson, L., Craig, A., Rodrigue, M., Titschack, J., Kolodziej, G., Abdulla, A., 2022. Discovery of the deep-sea NEOM Brine Pools in the Gulf of Aqaba, Red Sea. Commun Earth Environ 3, 146. https://doi.org/10.1038/s43247-022-00482-x.
R core team, 2022. R: a language and environment for statistical computing https://www.R-project.org/. R Foundation for Statistical Computing.
Reeder, D.B., Ma, B.B., Yang, Y.J., 2011. Very large subaqueous sand dunes on the upper continental slope in the South China Sea generated by episodic, shoaling deep-water internal solitary waves. Mar. Geol. 279, 12–18. https://doi.org/10.1016/j.margeo.2010.10.009.
Reimer, P.J., Baillie, M.G.L., Bard, E., Bayliss, A., Beck, J.W., Blackwell, P.G., Bronk Ramsey, C., Buck, C.E., Burr, G.S., Edwards, R.L., Friedrich, M., Grootes, P.M., Guilderson, T.P., Hajdas, I., Heaton, T.J., Hogg, A.G., Hughen, K.A., Kaiser, K.F., Kromer, B., McCormac, F.G., Manning, S.W., Reimer, R.W., Richards, D.A., Southon, J.R., Talamo, S., Turney, C.S.M., van der Plicht, J., Weyhenmeyer, C.E., 2009. IntCal09 and Marine09 Radiocarbon Age Calibration Curves, 0–50,000 Years cal BP. Radiocarbon 51, 1111–1150. https://doi.org/10.1017/S0033822200034202.
Reston, T.J., von Huene, R., Dickmann, T., Klaeschen, D., Kopp, H., 2002. Frontal accretion along the western Mediterranean Ridge: the effect of Messinian evaporites on wedge mechanics and structural style. Mar. Geol. 186, 59–82. https://doi.org/10.1016/S0025-3227(02)00173-1.
Rimoldi, B., Alexander, J., Morris, S., 1996. Experimental turbidity currents entering density-stratified water: analogues for turbidites in Mediterranean hypersaline basins. Sedimentology 43, 527–540. https://doi.org/10.1046/j.1365-3091.1996.d01-21.x.
Rohling, E.J., Gieskes, W.W.C., 1989. Late Quaternary changes in Mediterranean intermediate water density and formation rate. Paleoceanography 4, 531–545. https://doi.org/10.1029/PA004i005p00531.
Rohling, E.J., Marino, G., Grant, K.M., 2015. Mediterranean climate and oceanography, and the periodic development of anoxic events (sapropels). Earth Sci. Rev. 143, 62–97. https://doi.org/10.1016/j.earscirev.2015.01.008.
Rothwell, R.G., Thomson, J., Kähler, G., 1998. Low-sea-level emplacement of a very large Late Pleistocene 'megaturbidite' in the western Mediterranean Sea. Nature 392, 377–380. https://doi.org/10.1038/32871.
Ryan, W.B.F., Heezen, B.C., 1965. Ionian Sea Submarine Canyons and the 1908 Messina Turbidity current. GSA Bull. 76, 915–932.
Sagar, S., Esau, L., Hikmawan, T., Antunes, A., Holtermann, K., Stingl, U., Bajic, V.B., Kaur, M., 2013. Cytotoxic and apoptotic evaluations of marine bacteria isolated from brine-seawater interface of the Red Sea. BMC Complement. Altern. Med. 13, 29. https://doi.org/10.1186/1472-6882-13-29.
Salama, A., Meghraoui, M., El Gabry, M., Maouche, S., Hussein, M.H., Korrat, I., 2018. Paleotsunami deposits along the coast of Egypt correlate with historical earthquake records of eastern Mediterranean. Nat. Hazards Earth Syst. Sci. 18, 2203–2219. https://doi.org/10.5194/nhess-18-2203-2018.
Salamon, A., Rockwell, T., Ward, S.N., Guidoboni, E., Comastri, A., 2007. Tsunami hazard evaluation of the eastern mediterranean: historical analysis and selected modeling. Bull. Seismol. Soc. Am. 97, 705–724. https://doi.org/10.1785/0120060147.
Saltogianni, V., Mouslopoulou, V., Oncken, O., Nicol, A., Gianniou, M., Mertikas, S., 2020. Elastic fault interactions and earthquake rupture along the southern hellenic subduction plate interface zone in Greece. Geophys. Res. Lett. 47. https://doi.org/10.1029/2019GL086604.
Sawyer, D.E., Mason, R.A., Cook, A.E., Portnov, A., 2019. Submarine landslides induce massive waves in subsea brine pools. Sci. Rep. 9, 128. https://doi.org/10.1038/s41598-018-36781-7.
Schmidt, M., Al-Farawati, R., Botz, R., 2015. Geochemical Classification of Brine-Filled Red Sea Deeps. pp. 219–233. doi: 10.1007/978-3-662-45201-1_13.
Sgarrella, F., Moncharmont Zei, M., 1993. Benthic Foraminifera of the Gulf of Naples (Italy): systematics and autoecology. Bollettino Della Società Paleontologica Italiana 32, 145–264.
Shanmugam, G., 2012. Process-sedimentological challenges in distinguishing paleotsunami deposits. Nat. Hazards 63, 5–30. https://doi.org/10.1007/s11069-011-9766-z.
Shaw, B., Ambraseys, N.N., England, P.C., Floyd, M.A., Gorman, G.J., Higham, T.F.G., Jackson, J.A., Nocquet, J.-M., Pain, C.C., Piggott, M.D., 2008. Eastern Mediterranean tectonics and tsunami hazard inferred from the AD 365 earthquake. Nat. Geosci. 1, 268–276. https://doi.org/10.1038/ngeo151.
Shetty, S.A., Lathi, L., 2019. Microbiome data science. J Biosci (Rajshari) 445, 115.
Stevenson, A., Burkhardt, J., Cockell, C.S., Cray, J.A., Dijksterhuis, J., Fox-Powell, M., Kee, T.P., Kminek, G., McGenity, T.J., Timmis, K.N., Timson, D.J., Voytek, M.A., Westall, F., Yakimov, M.M., Hallsworth, J.E., 2015. Multiplication of microbes below 0.690 water activity: implications for terrestrial and extraterrestrial life. Environ. Microbiol. 17, 257–277. https://doi.org/10.1111/1462-2920.12598.
Stiros, S.C., 2001. The AD 365 Crete earthquake and possible seismic clustering during the fourth to sixth centuries AD in the Eastern Mediterranean: a review of historical and archaeological data. J. Struct. Geol. 23, 545–562. https://doi.org/10.1016/S0191-8141(00)00118-8.
Stuiver, M., Reimer, P.J., 1993. CALIB rev. 8. Radiocarbon 35, 215–230.
Ten Haven, H., de Lange, G.J., Klaver, G.T., 1985. The chemical composition and origin of the Tyro brine, eastern Mediterranean. A Tentative Model. Mar. Geol. 64, 337–342. https://doi.org/10.1016/0025-3227(85)90111-2.
Tesi, T., Miserocchi, S., Goñi, M.A., Langone, L., Boldrin, A., Turchetto, M., 2007. Organic matter origin and distribution in suspended particulate materials and surficial sediments from the western Adriatic Sea (Italy). Estuar. Coast. Shelf Sci. 73, 431–446. https://doi.org/10.1016/j.ecss.2007.02.008.
Tesi, T., Muschitiello, F., Smittenberg, R.H., Jakobsson, M., Vonk, J.E., Hill, P., Andersson, A., Kirchner, N., Noormets, R., Dudarev, O., Semiletov, I., Gustafsson, Ö., 2016. Massive remobilization of permafrost carbon during post-glacial warming. Nat. Commun. 7, 13653. https://doi.org/10.1038/ncomms13653.
Tiberti, M.M., Basili, R., Vannoli, P., 2014. Ups and downs in western Crete (Hellenic subduction zone). Sci. Rep. 4, 5677. https://doi.org/10.1038/srep05677.
Van Der Wielen, P.W.J.J., Bolhuis, H., Borin, S., Daffonchio, D., Corselli, C., Giuliano, L., D'Auria, G., de Lange, G.J., Huebner, A., Varnavas, S.P., Thomson, J., Tamburini, C., Marty, D., McGenity, T.J., Timmis, K.N., 2005. the enigma of prokaryotic life in deep hypersaline anoxic basins. Science 1979 (307), 121–123. https://doi.org/10.1126/science.1103569.
Varrella, S., Tangherlini, M., Corinaldesi, C., 2020. Deep hypersaline anoxic basins as untapped reservoir of polyextremophilic prokaryotes of biotechnological interest. Mar. Drugs 18, 91. https://doi.org/10.3390/md18020091.
Vengosh, A., de Lange, G.J., Starinsky, A., 1998. Boron isotope and geochemical evidence for the origin of Urania and Bannock brines at the eastern Mediterranean: effect of water-rock interactions. Geochim. Cosmochim. Acta 62, 3221–3228. https://doi.org/10.1016/S0016-7037(98)00236-1.
Vengosh, A., Starinsky, A., Anati, D.A., 1994. The origin of Mediterranean interstitial waters—relics of ancient Miocene brines: a re-evaluation. Earth Planet. Sci. Lett. 121, 613–627. https://doi.org/10.1016/0012-821X(94)90095-7.
Vernant, P., Bilham, R., Szeliga, W., Drupka, D., Kalita, S., Bhattacharyya, A.K., Gaur, V. K., Pelgay, P., Cattin, R., Berthet, T., 2014. Clockwise rotation of the Brahmaputra Valley relative to India: Tectonic convergence in the eastern Himalaya, Naga Hills, and Shillong Plateau. J. Geophys. Res. Solid Earth 119, 6558–6571. https://doi.org/10.1002/2014JB011196.

von Huene, R., Ranero, C.R., 2003. Subduction erosion and basal friction along the sediment-starved convergent margin off Antofagasta. Chile. J Geophys Res Solid Earth 108. https://doi.org/10.1029/2001JB001569.

von Huene, R., Reston, T., Kukwski, N., Dehghani, G.A., Weinrebe, W., 1997. A subducting seamount beneath the Mediterranean Ridge. Tectonophysics 271, 249–261. https://doi.org/10.1016/S0040-1951(96)00241-7.

Wallmann, K., Aghib, F.S., Castradori, D., Cita, M.B., Suess, E., Greinert, J., Rickert, D., 2002. Sedimentation and formation of secondary minerals in the hypersaline Discovery Basin, eastern Mediterranean. Mar. Geol. 186, 9–28. https://doi.org/10.1016/S0025-3227(02)00170-6.

Wallmann, K., Suess, E., Westbrook, G.H., Winckler, G., Cita, M.B., 1997. Salty brines on the Mediterranean sea floor. Nature 387, 31–32. https://doi.org/10.1038/387031a0.

Woodside, J.M., Volgin, A.V., 1996. Brine pools associated with Mediterranean Ridge mud diapirs: an interpretation of echo-free patches in deep tow sidescan sonar data. Mar. Geol. 132, 55–61. https://doi.org/10.1016/0025-3227(95)00153-0.

Yakimov, M.M., La Cono, V., Slepak, V.Z., La Spada, G., Arcadi, E., Messina, E., Borghini, M., Monticelli, L.S., Rojo, D., Barbas, C., Golyshina, O.V., Ferrer, M., Golyshin, P.N., Giuliano, L., 2013. Microbial life in the Lake Medee, the largest deep-sea salt-saturated formation. Sci. Rep. 3, 3554. https://doi.org/10.1038/srep03554.

Yakimov, M.M., La Cono, V., Spada, G.L., Bortoluzzi, G., Messina, E., Smedile, F., Arcadi, E., Borghini, M., Ferrer, M., Schmitt-Kopplin, P., Hertkorn, N., Cray, J.A., Hallsworth, J.E., Golyshin, P.N., Giuliano, L., 2015. Microbial community of the deep-sea brine Lake Kryos seawater–brine interface is active below the chaotropicity limit of life as revealed by recovery of mRNA. Environ. Microbiol. 17, 364–382. https://doi.org/10.1111/1462-2920.12587.

Zhou, Y., Gutiérrez-Preciado, A., Liu, Y., Moreira, D., Yakimov, M.M., López-García, P., Krupovic, M., 2025. Nested parasitism in hypersaline environments: viruses and virus satellites of haloarchaea and their nanosized cellular symbionts. doi: 10.1101/2025.02.15.638363.

Ziko, L., Saqr, A.-H.-A., Ouf, A., Gimpel, M., Aziz, R.K., Neubauer, P., Siam, R., 2019. Antibacterial and anticancer activities of orphan biosynthetic gene clusters from Atlantis II Red Sea brine pool. Microb. Cell Fact. 18, 56. https://doi.org/10.1186/s12934-019-1103-3.